Dynamic Interfacial Bond Behaviour between Basalt Fiber Reinforced Polymer Sheets and Concrete

Cheng Yuan[1], Wensu Chen[1], Thong M. Pham[1], Hong Hao[1] *, Cui Jian[2], Yanchao Shi[2]

[1]*Centre for Infrastructural Monitoring and Protection, School of Civil and Mechanical Engineering, Curtin University, Australia*

[2]*Tianjin University and Curtin University Joint Research Center of Structure Monitoring and Protection, School of Civil Engineering, Tianjin University, China*

**Corresponding Author*

Abstract

An experimental investigation on the dynamic interfacial bond behaviour between basalt fibre (BFRP) sheets and concrete under different loading speeds (i.e. 8.33E-6 m/s, 0.1 m/s, 1 m/s, 3 m/s, 5 m/s, and 8 m/s) by using single-lap shear tests was carried out in this study. Experimental results including bond strength, strain time histories, strain distributions in the bonding areas, interfacial fracture energy, and bond-slip curves are presented in this study. The test results show that the interface is strain rate dependent. The interfacial fracture energy, bond strength, and interfacial bond shear stress-slip are sensitive to strain rate. Empirical bond-slip model including strain rate effect are established for the predictions of bond properties between BFRP sheets and concrete under dynamic loadings.

Keywords: Basalt fibre-reinforced polymer (BFRP); Interfacial bond behaviour; Dynamic loads; Strain rate; DIC.

1. Introduction

Fibre-reinforced polymer (FRP), as an effective strengthening composite with high strength to weight ratio and excellent corrosion resistance, has been widely used to strengthen existing reinforced-concrete (RC) structures [1-4]. The interfacial bond between FRP and strengthened element is the dominated factor in determining the efficiency of the strengthening [5-9]. Numerous researches have been conducted to investigate the bond behaviour of FRP-to-concrete interface, and some empirical models have been proposed for bond strength and bond-slip relationship [10-12]. Mechanical properties of concrete, FRP, and adhesive resin are the main factors determining the interfacial bond capacity between FRP and strengthened element [13, 14].

However, the existing studies on the interfacial bond focus primarily on the static loading conditions [13, 15-20]. During the service life of civil engineering structures, it is likely to be subjected to dynamic loadings, such as seismic, impact, and blast loadings. A few studies [21-26] have reported that FRP strengthening is effective in enhancing structures to resist impact and blast loadings. It is noted that the mechanical properties of concrete and FRP are strain rate dependent [27, 28]. Since there is less time for damage to develop under high strain rate, material can sustain higher load and rupture strain due to the reduced accumulated damage at a particular strain level [29]. All the dynamic strength, the dynamic fracture strain and the dynamic Young's modulus of concrete are higher than the corresponding static values [30].

A few studies on the bond behaviour of FRP-to-concrete interface under low strain rate have been reported [31-33]. Shi et al. [31] implemented an experimental study on FRP-to-concrete joints and found that the interfacial bond was strain rate dependent, and the ultimate debonding strain and the peak shear stress increased with the strain rate. The strain rate considered in the latter study was relatively low and less than 0.1 s^{-1}. Shen et al. [32] implemented an experimental study and concluded that the effective bond length decreased, and shear stress enhanced with strain rate. The peak strain rate considered was 0.63 s^{-1} in the study. Huo et al. [33] experimentally tested the FRP-strengthened RC beam under impact loading and it was found that the loading rate remarkably influenced the bond strength while moderately affected the effective bond length. The maximum strain rate in the study was about 4.9 s^{-1}. An experimental study on BFRP-to-SFRC subjected to high strain rate conducted by Yuan et al. [34] found that the interfacial shear resistance and shear stress enhanced remarkably compared to the quasi-static tests.

Since the strain rate under impact and blast can reach up to 100 s^{-1} or even higher, it is necessary to carry out experimental study on the dynamic interfacial bond performance of FRP-to-concrete interface under higher strain rate. In order to obtain a higher strain rate, this study adopted various loading speeds to simulate the high strain rate. The maximum strain rate of BFRP sheet surface measured in this study was 155.1 s^{-1} under the loading speed of 8 m/s. To better understand the dynamic responses of the interfacial bond, dynamic testing results are compared with the results obtained from quasi-static tests, such as failure modes, strain distribution, interfacial shear stress, fracture energy, and bond strength. Meanwhile, an empirical dynamic model was proposed according to the testing data.

2. Experimental program

2.1 Material properties

The dimensions of concrete blocks were given as follows: the length was 150 mm, the width was 150 mm and the height was 300 mm, as shown in Figure 1. Concrete blocks with 30.14 MPa compressive strength and 2.89 MPa tensile strength were prepared in this study. The maximum coarse aggregate size of 10 mm was used in the concrete preparation. For the uni-directional basalt fiber (BFRP) sheet, the unit weight was 300 g/m^2; the nominal thickness was 0.12 mm; the tensile strength was 1333 MPa; the elastic modulus was 73 GPa; and the rupture strain was 1.88%. The adhesive consisting two parts (i.e. epoxy resin and hardener) with a ratio of 5:1 has a rupture tensile strength of 50.5 MPa, elastic modulus of 2.8 GPa and rupture strain of 4.5%.

2.2 Test setup

The single-lap shear tests (SST) were carried out by using Instron VHS 160-20 high speed servo hydraulic testing machine. This machine is able to provide constant velocity in the range of 0.1 m/s to 25 m/s. Figure 1 illustrates the specimen details and Figure 2 shows the testing machine and experimental setup. Twenty-seven specimens were tested with three specimens for each configuration in total. **Table 1** summarizes the details of the specimens and the testing data. It should be noted that n_f refers to the number of BFRP layers, L represents the bonding length of BFRP sheets, b_f refers to the bond width of BFRP sheets, s^{-1} is the measured strain rate, P_u represents the debonding loads, τ_m refers to the peak shear stress (PSS), s_o refers to the slip at the peak shear stress, G_f is the interfacial fracture energy (IFE), and L_e refers to the effective bond length (EBL).

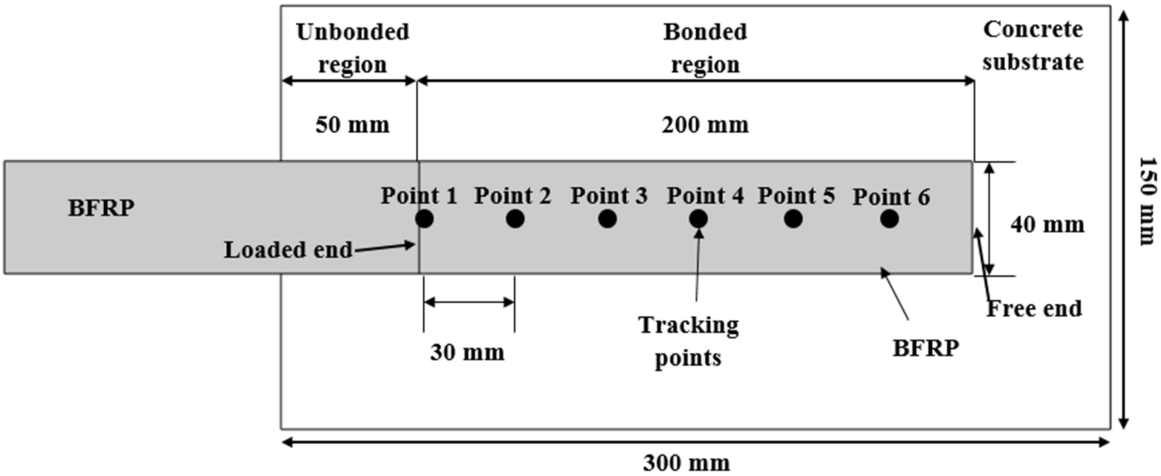

Figure 1. Specimen detail

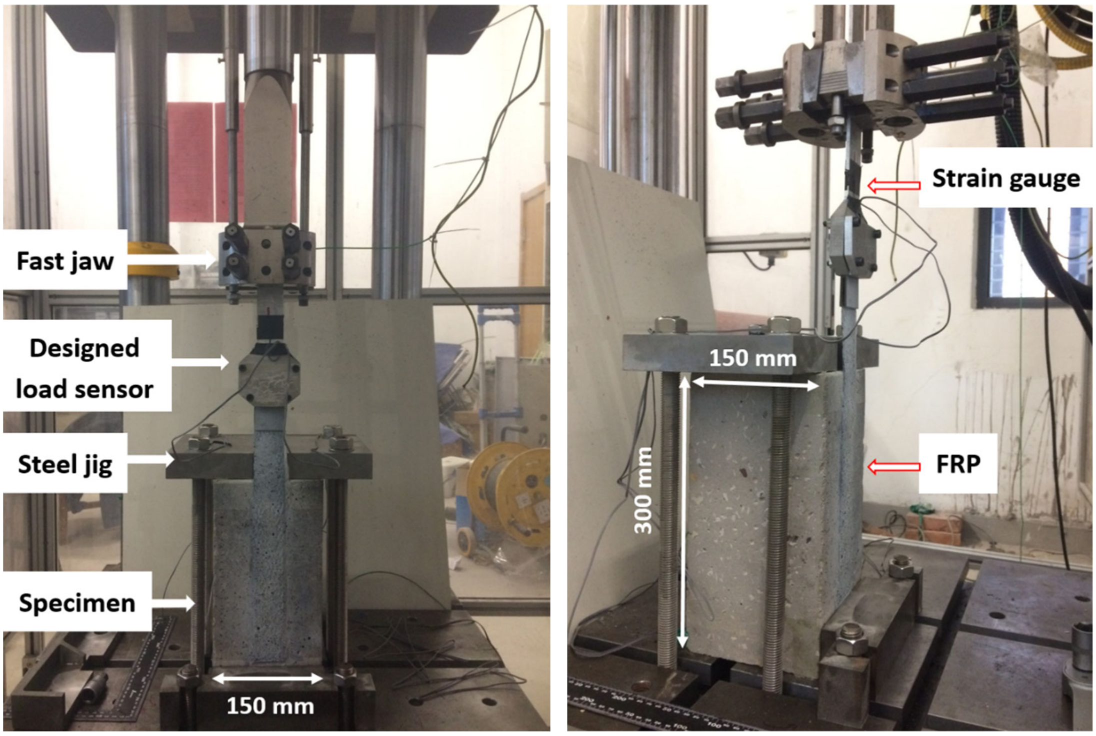

(a) SST: (L) Front view; (R) Side view

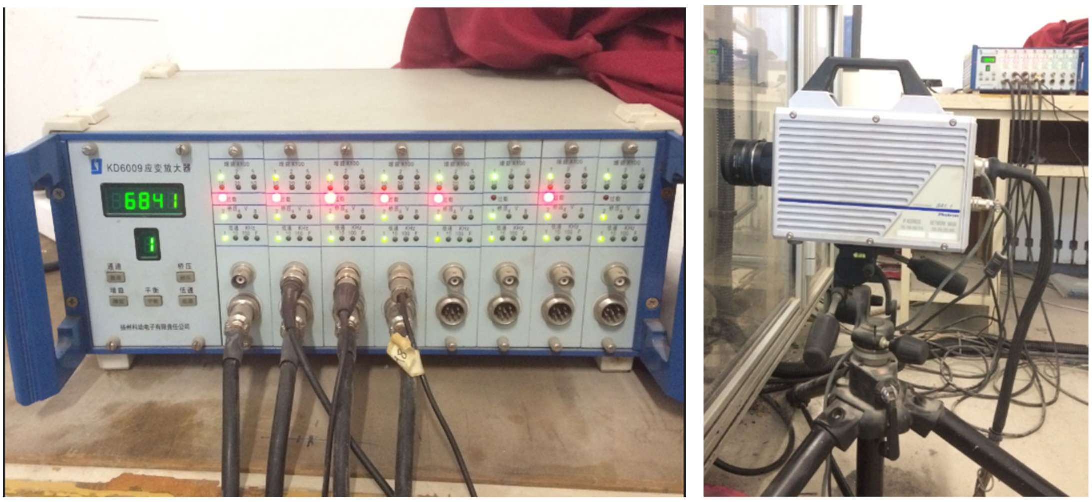

(b) Test instruments: (L) Strain amplifier; (R) High speed camera

Figure 2. Test setup and instruments

Table 1. Details of the specimens and main results for the static and dynamic tests

Specimen ID	n_f	L (mm)	b_f (mm)	Loading speed (m/s)	s^{-1}	P_u (kN)	τ_m (MPa)	s_o (mm)	G_f (N/mm)	A (%)	B (mm^{-1})	Le (mm)	$f_{t,DIF}$ (MPa)	Failure mode
QS_1	2	200	40	8.33E-6	2.50E-5	6.93	2.11	0.146	0.89	1.009	4.737	96	/	C
QS_2	2	200	40	8.33E-6	2.50E-5	7.87	2.20	0.131	0.70	0.897	4.897	89	/	C
QS_3	4	200	40	8.33E-6	2.50E-5	9.04	2.72	0.125	0.98	0.746	5.534	105	/	C
QS_4	4	200	40	8.33E-6	2.50E-5	8.65	2.80	0.133	1.07	0.780	5.210	96	/	C
QS_5	2	200	25	8.33E-6	2.50E-5	4.12	2.21	0.109	0.88	1.002	6.368	85	/	C
QS_6	2	200	25	8.33E-6	2.50E-5	3.69	1.97	0.138	0.78	0.946	5.021	80	/	C
D1_0.1MPS_1	2	200	40	0.1	4.50	7.00	2.95	0.131	1.11	1.128	5.295	94	3.27	C
D1_0.1MPS_2	2	200	40	0.1	4.20	7.80	2.67	0.129	0.99	1.066	5.372	87	3.21	C
D1_0.1MPS_3	2	200	40	0.1	4.11	8.08	2.65	0.139	1.06	1.103	4.978	92	3.19	C
D2_1MPS_1	2	200	40	1.0	25.80	8.01	5.34	0.130	2.00	1.512	5.331	66	5.20	C
D2_1MPS_2	2	200	40	1.0	33.20	8.02	4.89	0.131	1.84	1.452	5.297	55	5.53	C
D2_1MPS_3	2	200	40	1.0	29.40	8.40	4.85	0.125	1.75	1.415	5.541	78	5.37	C
D3_3MPS_1	2	200	40	3.0	46.60	9.91	7.03	0.119	2.41	1.661	5.815	59	6.00	C
D3_3MPS_2	2	200	40	3.0	53.50	9.50	6.85	0.127	2.51	1.694	5.457	65	6.20	C/CE
D3_3MPS_3	2	200	40	3.0	54.30	10.01	7.25	0.109	2.29	1.620	6.312	66	6.22	C/CE
D4_5MPS_1	2	200	40	5.0	103.10	12.00	8.66	0.099	2.49	1.688	6.947	48	7.19	C/CE
D4_5MPS_2	2	200	40	5.0	104.80	9.01	7.65	0.110	2.44	1.670	6.265	55	7.22	C/CE
D4_5MPS_3	2	200	40	5.0	101.60	13.12	8.64	0.101	2.51	1.693	6.879	50	7.17	C/CE
D5_8MPS_1	2	200	40	8.0	155.10	15.03	9.55	0.100	2.85	1.781	6.875	45	7.85	C/CE
D5_8MPS_2	2	200	40	8.0	150.10	12.95	9.05	0.099	2.60	1.726	6.939	48	7.80	C/CE
D5_8MPS_3	2	200	40	8.0	130.40	11.02	9.82	0.097	2.75	1.774	7.125	50	7.57	C/CE
D6_5MPS_1	4	200	40	5.0	98.70	15.62	8.47	0.101	2.47	1.182	6.860	42	7.12	C/CE
D6_5MPS_2	4	200	40	5.0	94.50	14.59	9.24	0.102	2.73	1.241	6.786	40	7.05	C/CE
D6_5MPS_3	4	200	40	5.0	92.70	13.72	9.23	0.114	3.03	1.310	6.087	46	7.02	C/CE
D7_5MPS_1	2	200	25	5.0	98.57	8.29	6.53	0.128	2.43	1.665	5.378	61	7.12	C/CE
D7_5MPS_2	2	200	25	5.0	104.51	7.33	7.60	0.139	3.05	1.866	4.984	57	7.21	C/CE
D7_5MPS_3	2	200	25	5.0	108.72	7.24	6.01	0.133	2.67	1.745	5.198	75	7.27	C/CE

It should be noted that *C* refers to debonding due to concrete failure, *CE* refers to debonding in the interface of concrete-epoxy, *A* is the ultimate strain derived from the regression analysis, *B* refers to the stiffness index obtained from the regression analysis, and $f_{t,DIF}$ refers to the estimated dynamic tensile strength of concrete.

3. Experimental results and discussions

3.1 Failure mode

The failure modes under different loading speeds are shown in Figure 3. For the specimens under quasi-static loading and the dynamic loading speeds of 0.1 m/s, 1 m/s and 3 m/s, debonding occurred owing to the failure of concrete substrates and a thin layer of concrete was peeled off. In addition, the fracture path always penetrated through the aggregate-to-mortar interface, where is the interfacial transition zone (ITZ). However, under the higher loading speeds of 5 m/s and 8 m/s, the failure mode changed, as shown in Figure 3 (d), (e) and (f). The peel-off failure of concrete substrate is no longer uniform. More concrete detachment was observed near the loaded end. A small amount of adhesive layer, which is not very clear in the photos, was found on the detached concrete substrates close to the free end. These results show that the debonding failure not only occurred because of the concrete failure but also because of the failure of the concrete-epoxy interface, and the failure was not uniform along the bonded area. This indicates that the debonding failure was sensitive to the loading speed. The might be due to the interfacial transition zone between aggregate and mortar is strong enough under higher strain rate because of the enhanced concrete tensile strength. In general, high speed loading leads to two possible debonding failure modes: (1) concrete failure (C) and (2) concrete-epoxy (CE) interface failure. The cracking resistance of concrete and rupture resistance of epoxy are enhanced under dynamic loadings. The debonding initiated from the weaker layer of two interfaces (i.e. C and CE).

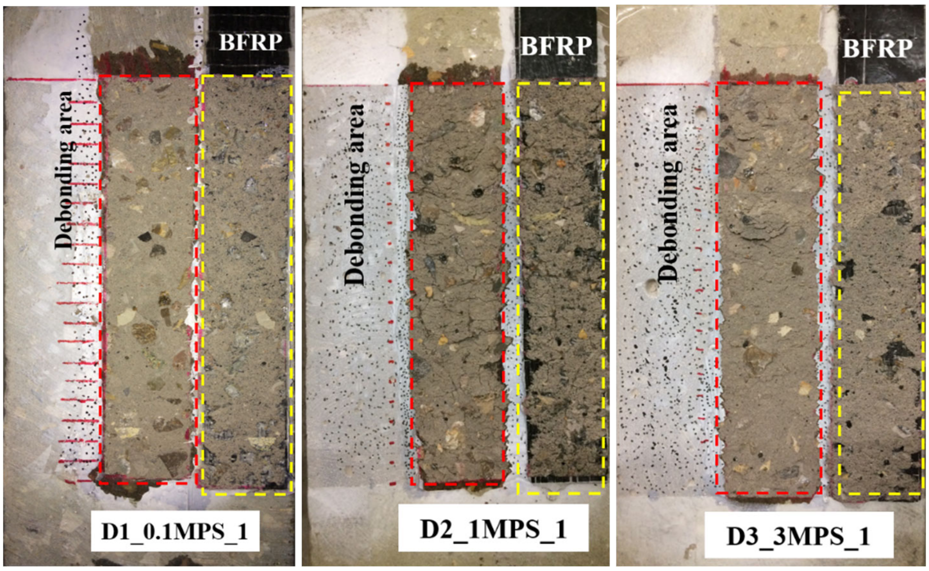

(a) D1_0.1MPS_1 (b) D2_1MPS_1 (c) D3_3MPS_1

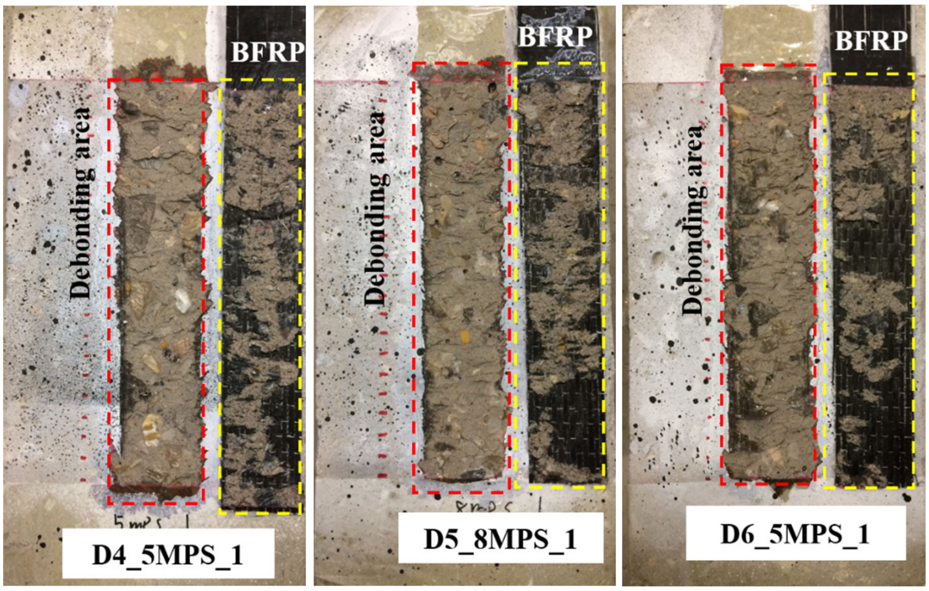

(d) D4_5MPS_1 (e) D5_8MPS_1 (f) D6_5MPS_1

Figure 3. Failure modes under different loading speeds

3.2 Load-slip relationship

Digital image correlation (DIC) technique was used to measure the fields of displacement and strain of the Region of Interest (ROI), which is shown in Figure 4. The reliability of the DIC technique is verified against actual reading from strain gauges as proven in the previous study by Yuan et al. [35]. Due to ringing effect, severe oscillation may be observed in the measured load-time curves. The system ringing in dynamic tests is a common phenomenon and cannot be eliminated if contact measurement method is adopted [36, 37]. Therefore, DIC as the non-contact measurement method was used to mitigate the vibration effect. The ROI consists of two parts, one is the unbonded part which is reserved to eliminate the edge effect of concrete, and the other region is the bonded part with a bond length of 200 mm.

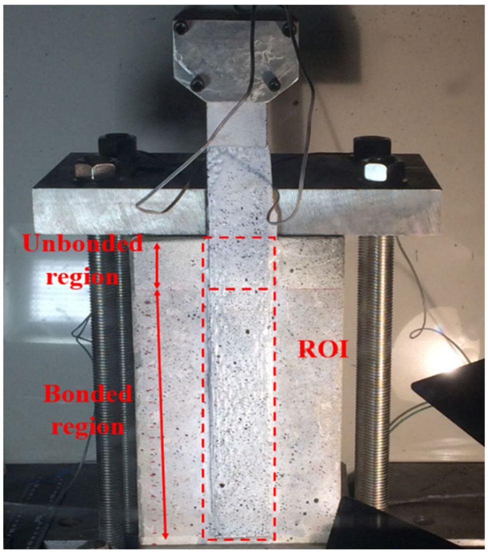

Figure 4. Region of interest (ROI)

Figure 5 illustrates the load-slip curves for all the tested specimens. As can be seen, the pattern of the load-slip curves has not been affected by the strain rate as elastic stage and debonding plateau under dynamic loadings are similar to that under quasi-static loading. The debonding load and ultimate slip increased with the loading velocity. As listed in **Table 1**, the average debonding loads of the specimens QS (i.e. QS_1 and QS_2), D1_0.1MPS, D2_1MPS, D3_3MPS, D4_5MPS, and D5_8MPS were 7.63 kN, 8.14 kN, 9.81 kN, 11.38 kN, 13.00 kN, and 14.64 kN, respectively. With the increasing strain rate from 2.59E-5 s^{-1} to 4.27 s^{-1}, 29.47 s^{-1}, 51.47 s^{-1}, 103.17 s^{-1}, and 155.10 s^{-1}, the dynamic debonding loads increased by 3.06%, 10.05%, 32.52%, 53.74%, and 97.88%, respectively. This indicates that the interfacial bond strength is enhanced due to the increased cracking resistance of concrete substrates under dynamic loadings. In addition, the ultimate slip increased as well with the rising strain rate, indicating that the debonding process under dynamic loadings is more ductile than that under quasi-static loadings. Up to the loading velocity of 3 m/s, the slip at debonding load was approximately 0.25 mm while the corresponding values for the cases of 5 m/s and 8 m/s were about 0.5 mm and 0.6 mm, respectively. This is because the BFRP sheets can experience more deformation during the microcracking stage and debonding process to overcome the enhanced interfacial bond strength under dynamic loadings. The increased debonding load and slip indicate that the ductility of the single-lap shear specimens increases with the strain rate. It should be noted that only two specimens were tested under quasi-static tests.

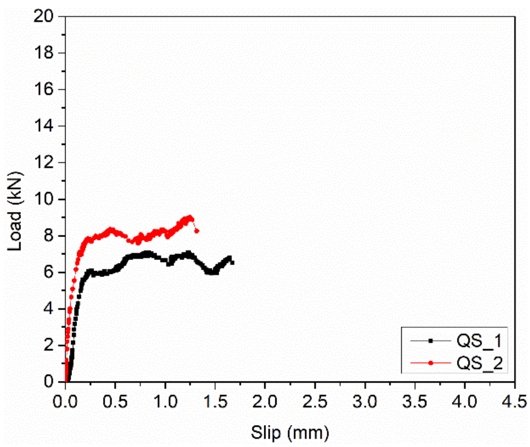

(a) QS_1 and 2

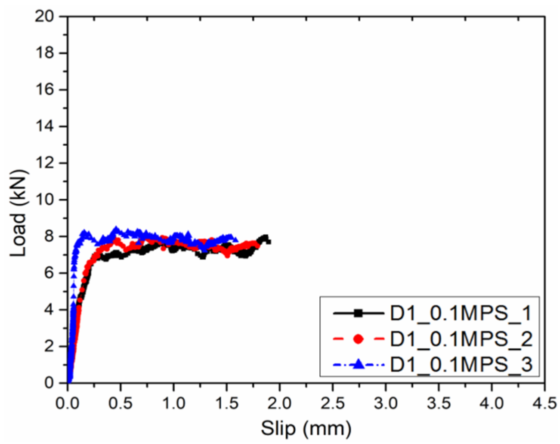

(b) D1_0.1MPS

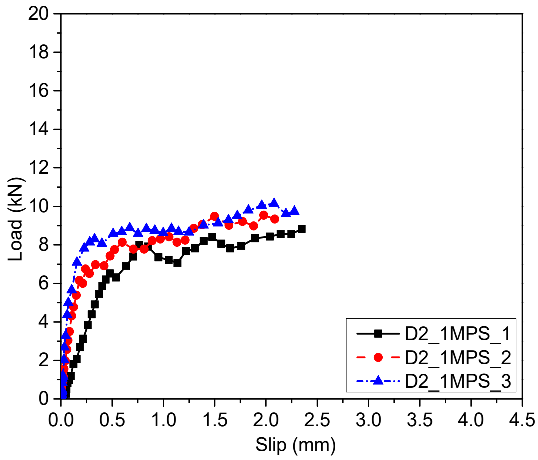

(c) D2_1MPS

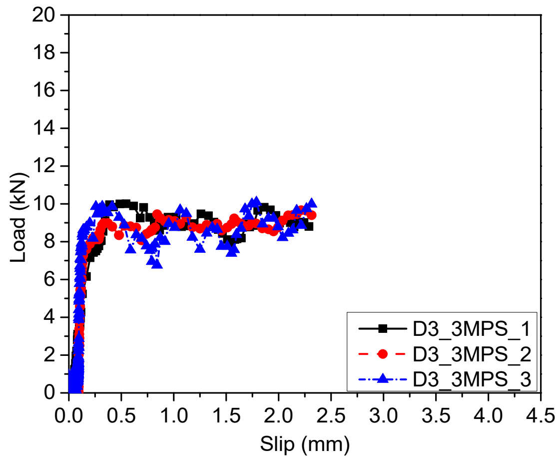

(d) D3_3MPS

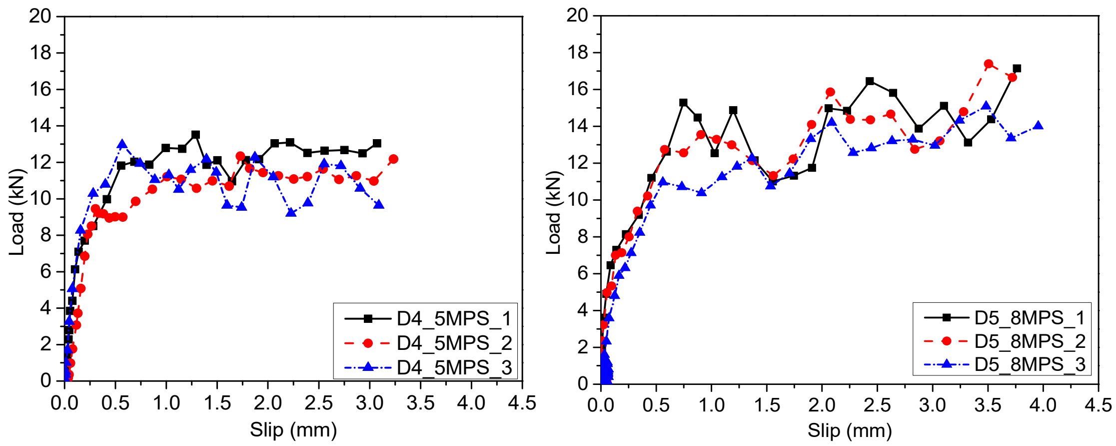

(e) D4_5MPS (f) D5_8MPS

Figure 5. Load and slip curves

3.3 Strain distribution

FRP strain profile of each specimen under different loading stages was derived by the DIC technique. Figure 6 illustrates the strain contours with different colours. Red and blue colours represent the maximum and minimum strain. The strain contours also provide the strain value and strain transfer length of BFRP sheets. Overall, similar patterns of strain distribution along the loading direction were observed. It seems that the pattern of strain fields was not affected by strain rate. With the increasing loading speed, more uniform strain distribution was observed in the ROI. For the specimens under the loading speeds of 8.33E-6 m/s and 0.1 m/s, non-uniform strain concentration was observed around the loaded end of the BFRP sheets at the beginning of loading, as shown in Figure 6 (a and b), indicating that the strain profile was marginally impacted by the strain rate because the cracking in the concrete layer had enough time to penetrate from the weak parts of the concrete under relatively lower loading speed (e.g. less than 0.1 m/s). The localization of strain indicates the concentration of shear stress in the red colour. The colours of yellow, green and light blue refer to the shear stress transition zone. The dark blue represents the non-stress transfer zone.

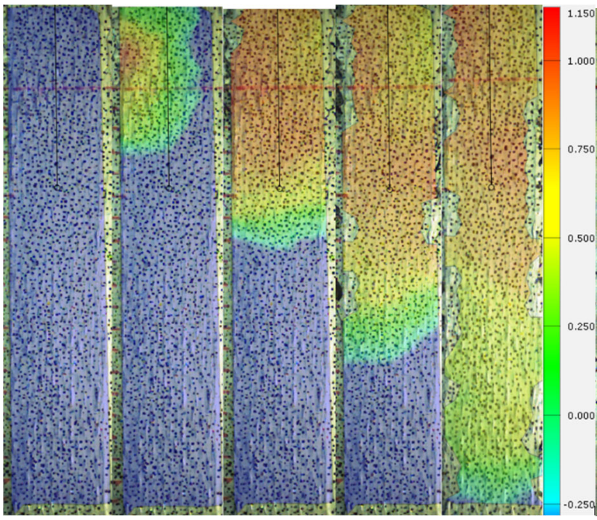

(a) QS_1

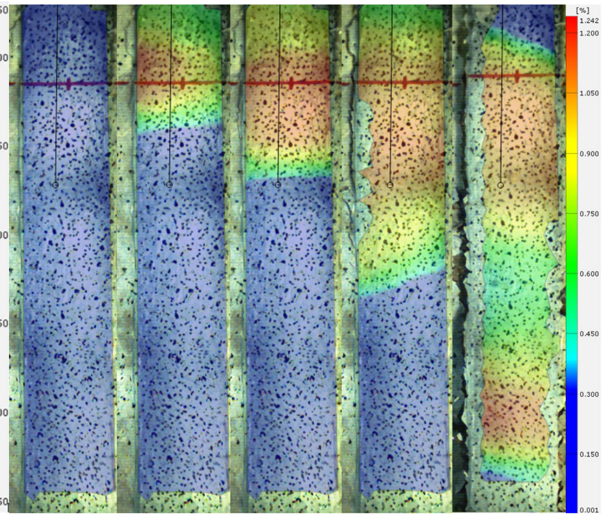

(b) D1_0.1MPS_1

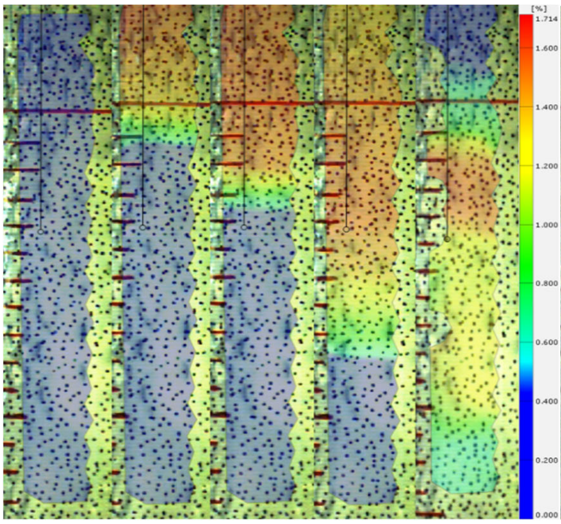

(c) D3_3MPS_1

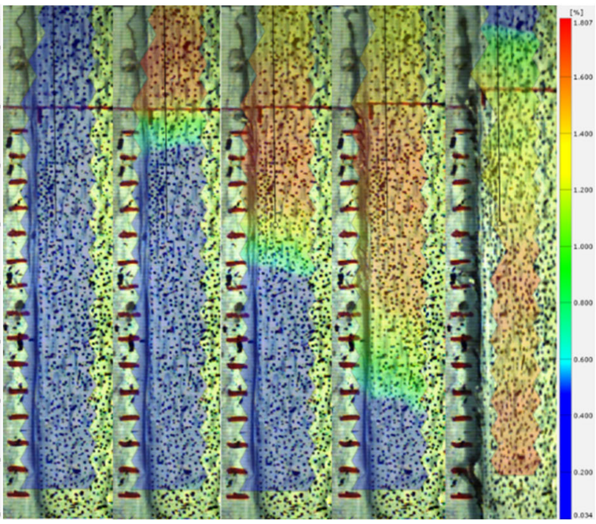

(d) D5_8MPS_1

Figure 6. Strain contours under different loading instants

Figure 7 plots the strain time histories of BFRP sheets at the selected six points indicated in Figure 1. The debonding initiated from Point 1 (closer to the loaded end) to Point 6 (closer to the free end), which is similar to the results under quasi-static loadings as reported by Baky et al. [38]. With the increase of loading speed, significantly higher ultimate debonding strain and shorter duration of loading time were obtained. As compared to the case of low loading speeds, the BFRP strain of specimens associated with high loading speeds raised much more rapidly. The FRP debonding strain raised with strain, indicating that the shear resistance of the BFRP-to-concrete interface was enhanced with the strain rate. In addition, changing the BFRP sheets from two layers (Figure 7d) to four layers (Figure 7f) resulted in the decrease of the strain under the same loading velocity of 5 m/s, indicating that the increased thickness of BFRP sheets reduced the strain development under dynamic loading.

To obtain dynamic stress equilibrium, at least three reverberations of the loading wave in the specimen are required for a uniaxial tensile test [39, 40]. To estimate the velocity of the stress wave, the equation $c=\sqrt{\frac{E}{\rho}}$ can be employed. However, the stress wave velocity of the FRP-to-concrete joints is not easy to estimate due to the two interfaces including BFRP-to-epoxy and epoxy-to-concrete in the FRP-to-concrete joints. The elastic modulus E and the density ρ cannot be confirmed due to the multiple interfaces. Thus, six points were selected from the BFRP sheets to compare the strain distributions at different instants of time, as shown in Figure 1 [41, 42]. As can be observed in Figure 7, once the strain of the first five selected points reaches the maximum value it remains almost a constant leading to a uniform strain distribution along the specimen, demonstrating that the dynamic SST satisfies the dynamic stress equilibrium. The reason for the different strain distribution of point 6 from the other points including the shape and value is because the point closer to the free end of FRP cannot develop the full debonding process due to the brittle behaviour.

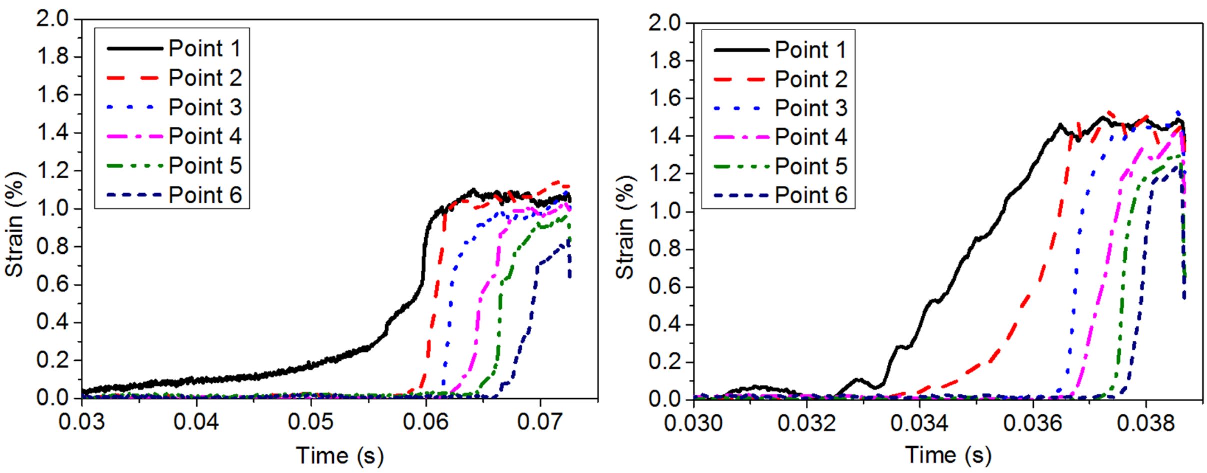

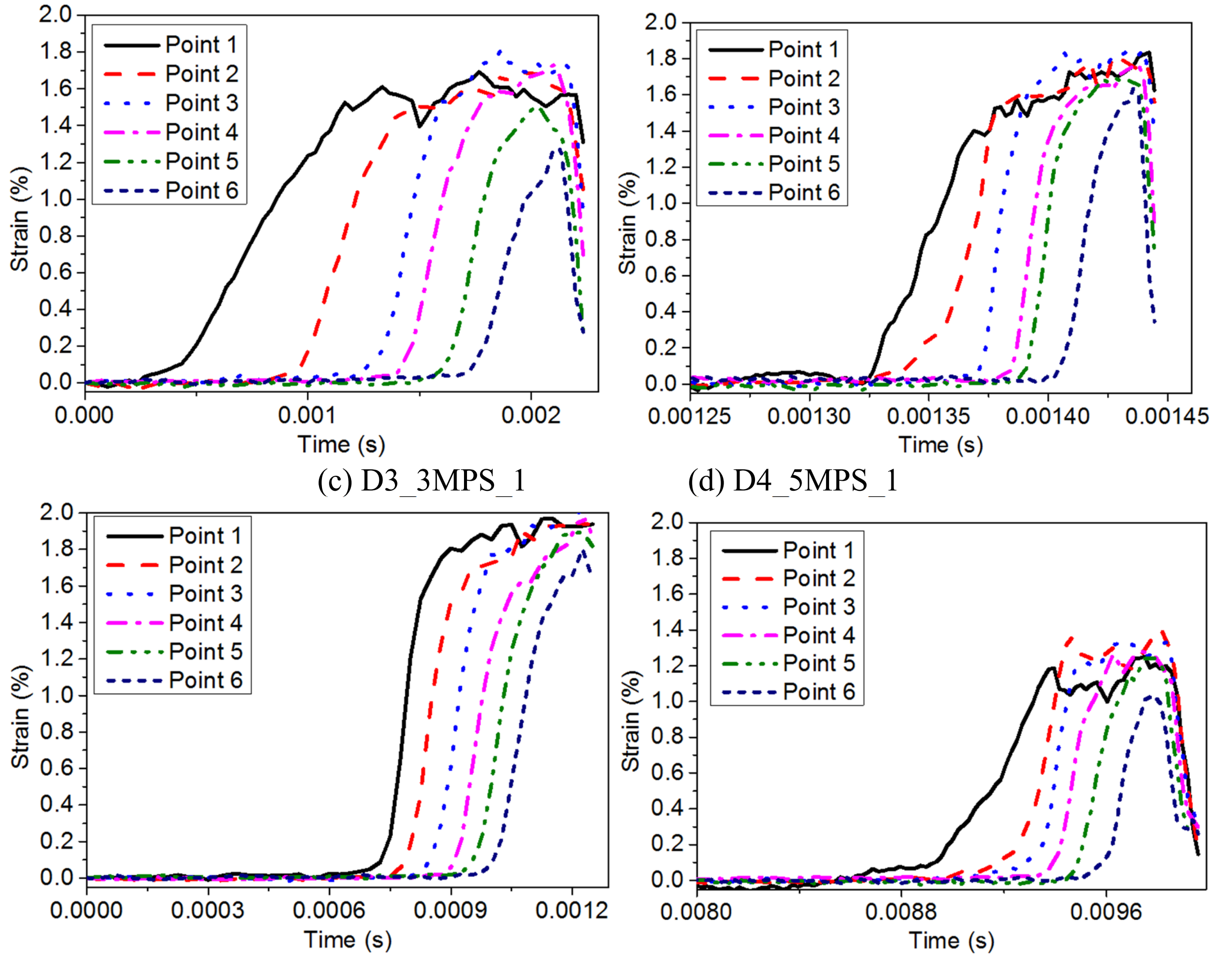

(a) D1_0.1MPS_1 (b) D2_1MPS_1

(c) D3_3MPS_1 (d) D4_5MPS_1

(e) D5_8MPS_1 (f) D6_5MPS_2

Figure 7. Strain-time histories

Figure 8 shows the strain distributions along the bond length of BFRP sheets at different loading levels. For all the specimens, the strain firstly increased with the applied loads. As the applied load reached the initial debonding stage (P_u), there was nearly no further increment of the strain. The strain distribution remained "*S*" profile to develop the debonding process. As shown in Figure 8, the FRP debonding strain significantly raised with the rising loading rate, and the larger shear stress transfer region can be observed when the ultimate load was achieved. In addition, the BFRP strain profile under higher loading speeds is steeper than that obtained with lower loading speeds, indicating that the enhanced shear resistance is obtained for BFRP-strengthened concrete joints under higher speed loadings. Figure 8 (d) and (f) shows the strain distributions by changing two layers of BFRP sheets to four layers under the same loading speed of 5 m/s. The measured results demonstrated that increasing BFRP stiffness significantly enhanced the shear resistance under dynamic loads. However, the loading speeds had marginal effect on the strain distribution gradient. The profile of the strain distribution subjected to dynamic loadings is similar to that under static tests, which has been also reported by Huo et al. [23].

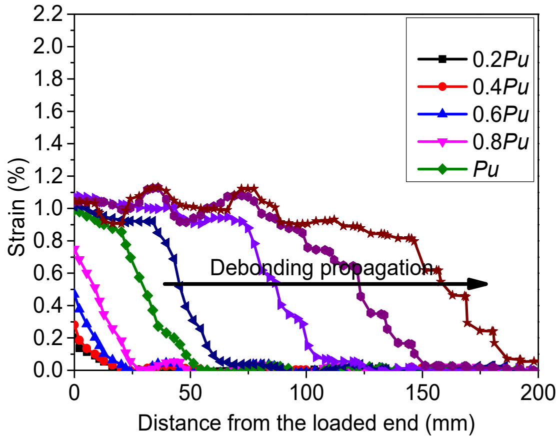

(a) D1_0.1MPS_1

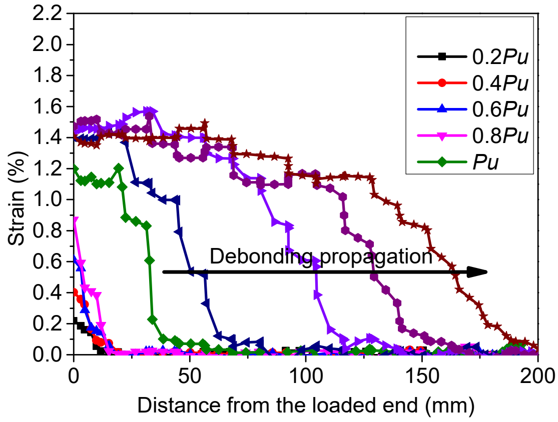

(b) D2_1MPS_1

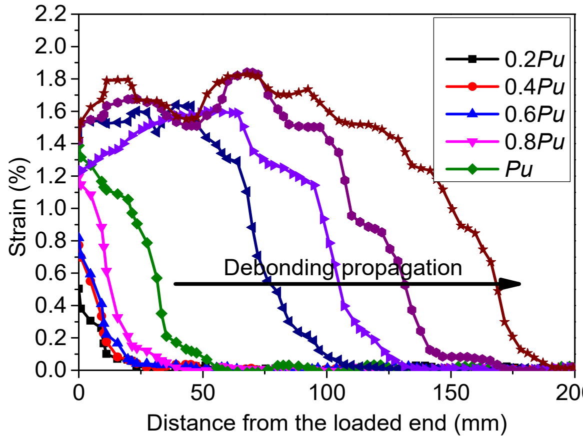

(c) D3_3MPS_1

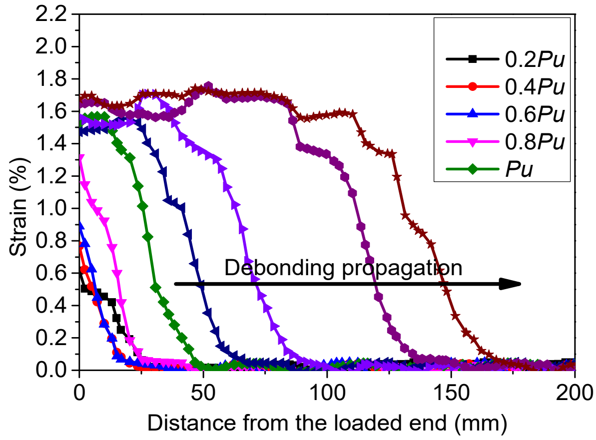

(d) D4_5MPS_1 (2 layers of BFRP sheets)

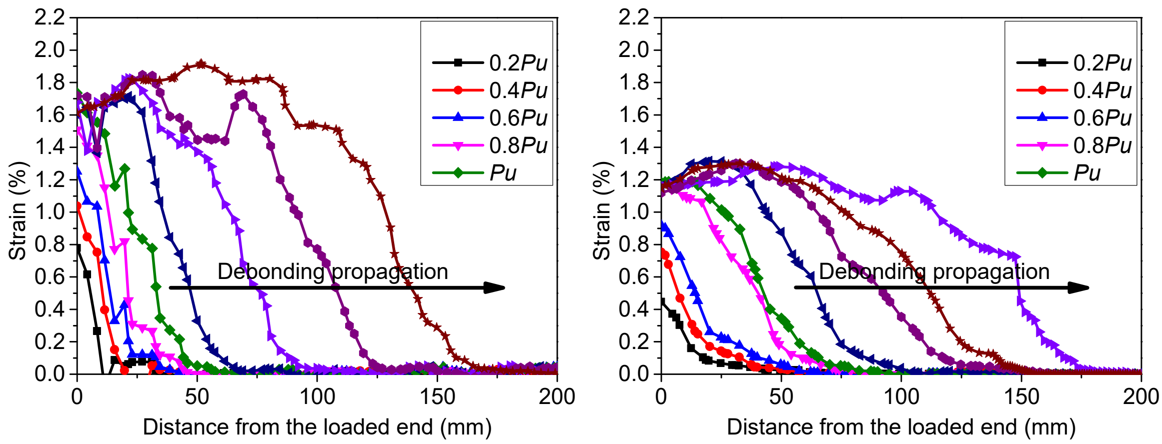

(e) D5_8MPS_1 (f) D6_5MPS_2 (4 layers of BFRP sheets)

Figure 8. Strain distributions under different loading speeds

Table 1 gives the maximum strain rate for all the tested specimens. The determination of strain rate in this study was based on the differentiation of strain time history, as given in Equation (1). In general, the peak strain rate increased with the loading speed. Figure 9 illustrates the relationship between strain rate and location at different time instants. The strain rates varied with time reaching the maximum strain rate and maintained its bell shape to propagate along the bonded length of BFRP sheets. The maximum strain rate was approximately 155.10 s^{-1} at the loading speed of 8 m/s while the strain rate was around 4 s^{-1} at the loading speed of 0.1 m/s.

$$\dot{\varepsilon} = \frac{d\varepsilon}{dt} \tag{1}$$

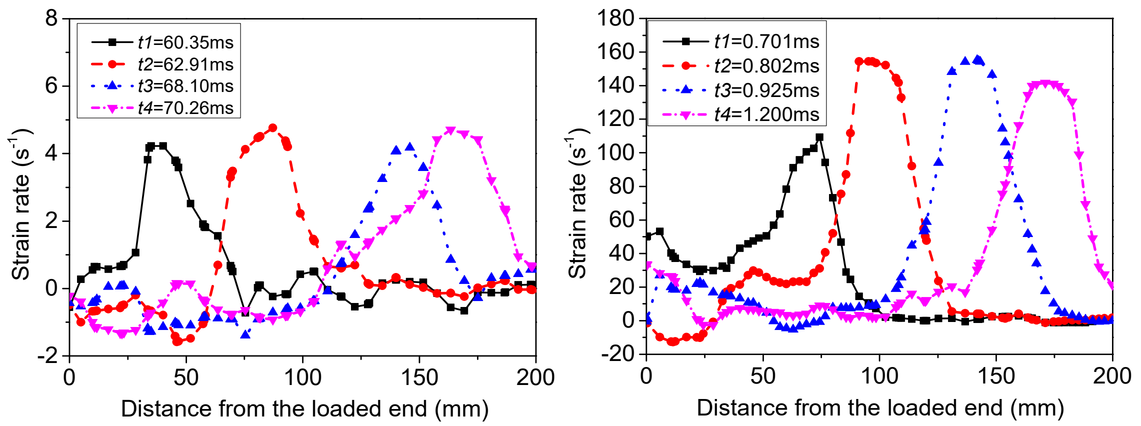

(a) D1_0.1MPS_1 (b) D5_8MPS_1

Figure 9. Strain rate distributions at different time instants

3.4 Strain-slip relationship

To obtain the interfacial bond-slip relationships between FRP and concrete, a non-linear fitting equation proposed by Dai et al. [16] was employed herein. Three sets of strain-slip curves corresponding to each specimen were adopted for regression analysis. Three points (i.e. Point 1, Point 2, and Point 3 as shown in Figure 1) near the loaded end of BFRP sheets were selected from the DIC, as shown in Figure 10. The points close to the free end were not selected because the points near the free end cannot represent the debonding behaviour of the points close to the loaded end due to the brittle debonding of the BFRP-to-concrete interface. As proposed by Dai et al. [43], the relationship between strain and slip can be expressed as follows [10, 16]:

$$\varepsilon = f(s) = A\left(1 - e^{-Bs}\right) \quad (2)$$

where A and B are the coefficients obtained from the fitted ε-s curves of experimental results, A is the ultimate debonding strain of the FRP with enough bond length, B refers to the stiffness index, which dominates the shape of the bond-slip curves [16].

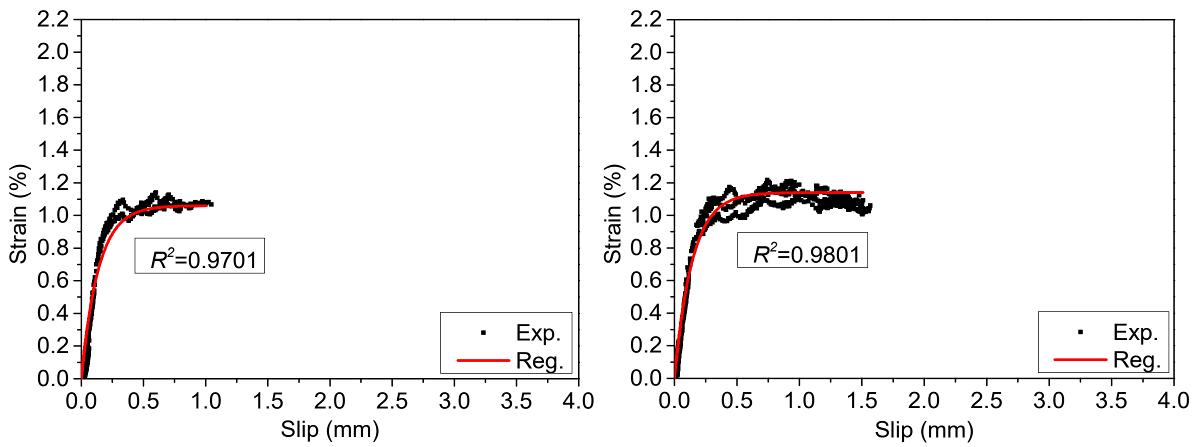

(a) QS_1 (b) D1_0.1MPS_1

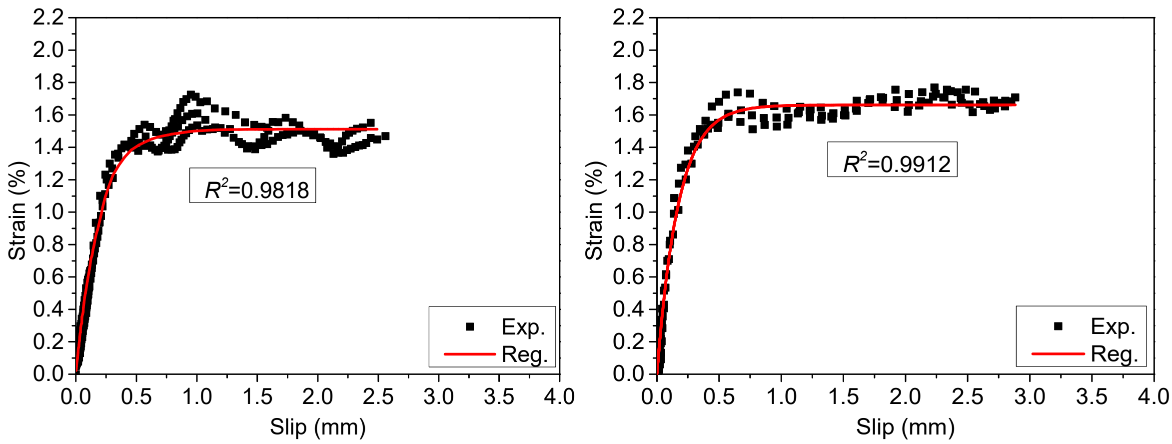

(c) D2_1MPS_1 (d) D3_3MPS_1

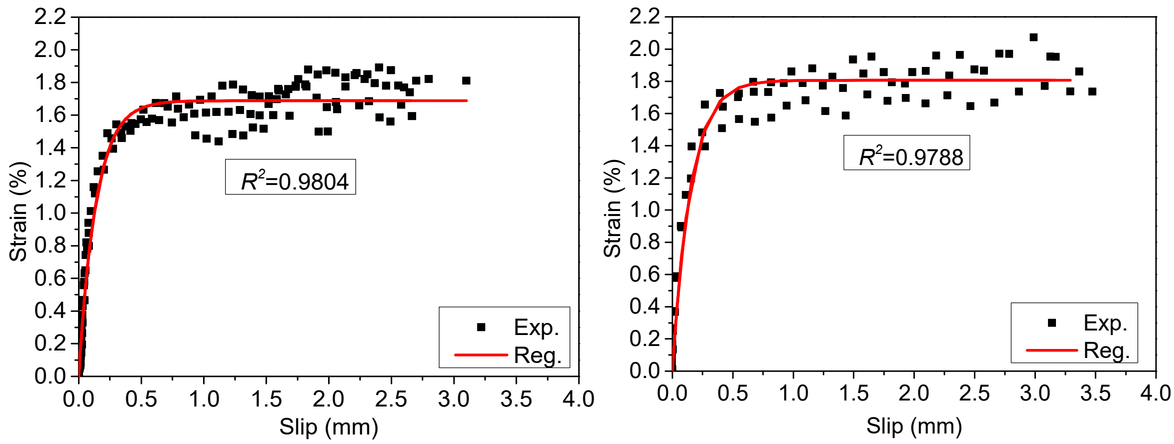

(e) D4_5MPS_1 (f) D5_8MPS_1

Figure 10. Strain-slip curves from the experimental results

The selected three points measured in these tests had similar strain-slip relationship, and the tested and regressed strain-slip curves show non-linear behaviour because of concrete cracking [44]. Figure 11 illustrates the relationship between bond-slip curve (R) and strain-slip curve (L). After regression analysis of the strain-slip curves, two parts can be obtained including part 1 (red colour) and part 2 (black colour). A nonlinear exponential function can be employed to describe the bond-slip curve due to the cracking of concrete layer during the debonding process [16].

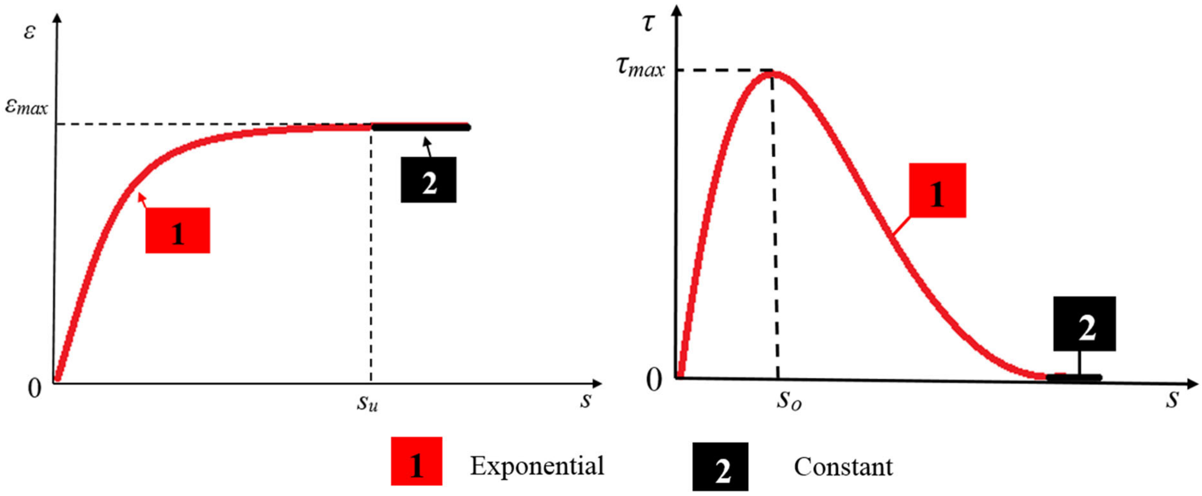

Figure 11. (L) Strain-slip curve; (R) Bond-slip curve

The coefficients *A* and *B* from regression analysis are listed in **Table 1**. The comparison of the best-fitted strain-slip curves is plotted in Figure 12 (L). With the rising loading rate, the BFRP strain and the ultimate slip raised significantly. The average ultimate debonding strains (i.e. *A*) of the specimens D1_0.1MPS, D2_1MPS, D3_3MPS, D4_5MPS, and D5_8MPS were 1.099%, 1.459%, 1.658%, 1.683%, and 1.760%, respectively. With the increasing strain rate from 2.50E-5 s^{-1} to 4.27 s^{-1}, 29.47 s^{-1}, 51.47 s^{-1}, 103.17 s^{-1}, and 155.10 s^{-1}, the dynamic debonding strains increased by 15.32%, 53.17%, 74.01%, 76.67%, and 84.12%, respectively, and the stiffness index *B* increased by 7.63%, 10.63%, 17.81%, 28.07%, and 30.99%, respectively. For the specimens subjected to dynamic loadings, a slight change in the initial interface stiffness can be observed in Figure 12. The improved initial stiffness indicates that the effect of strain rate on the interface was significant. The improved interfacial stiffness should be affected by the stiffness of concrete layer, the adhesive layer, and the FRP layer. Additionally, the bonding width of BFRP sheets has a limited effect on the interfacial stiffness except for the ultimate debonding strain under dynamic loading of 5 m/s by changing the BFRP width from 25 mm to 40 mm, as given in **Table 1** and as shown in Figure 12 (R). By increasing the BFRP layers from 2 to 4, the interfacial stiffness is slightly improved due to the increased average value of *B* but the ultimate debonding strain drops significantly in the tests. This indicates that the increased BFRP stiffness ($E_f t_f$) enhances the shear resistance of the BFRP-to-concrete interface under dynamic loading, which is consistent with the results under static loading as reported by Subramaniam et al. [45]. The interfacial stiffness K can be expressed as follows [46]:

$$K = \frac{1}{\frac{t_c}{G_c} + \frac{t_a}{G_a} + \frac{t_s}{G_s}} \tag{3}$$

$$G_i = \frac{E_i}{2(1+v_i)} \tag{4}$$

where G_c, G_a, and G_s are the shear modulus of concrete, adhesive, and FRP layer, respectively; t_c, t_a, and t_s are the thickness of the concrete, adhesive, and FRP layer, respectively; G_i is the shear modulus; and v_i is Poisson's ratio [47]. The interfacial stiffness improved significantly because Young's modulus of concrete is strain rate dependent [30, 48, 49]. Hao and Hao [49] proposed equations to define the strain rate effect on the Young's modulus of concrete. Chen et al. [50] proposed equations to describe the relation between strain rate and elastic modulus of BFRP sheets. Liao et al. [48] demonstrated the effect of strain rate on the tensile strength of epoxy. The interfacial stiffness K increased with the increase in G_c, G_a, and G_s according to Equations (3) and (4). It should be noted that the thickness of the concrete, adhesive, and FRP were assumed as a constant in this study.

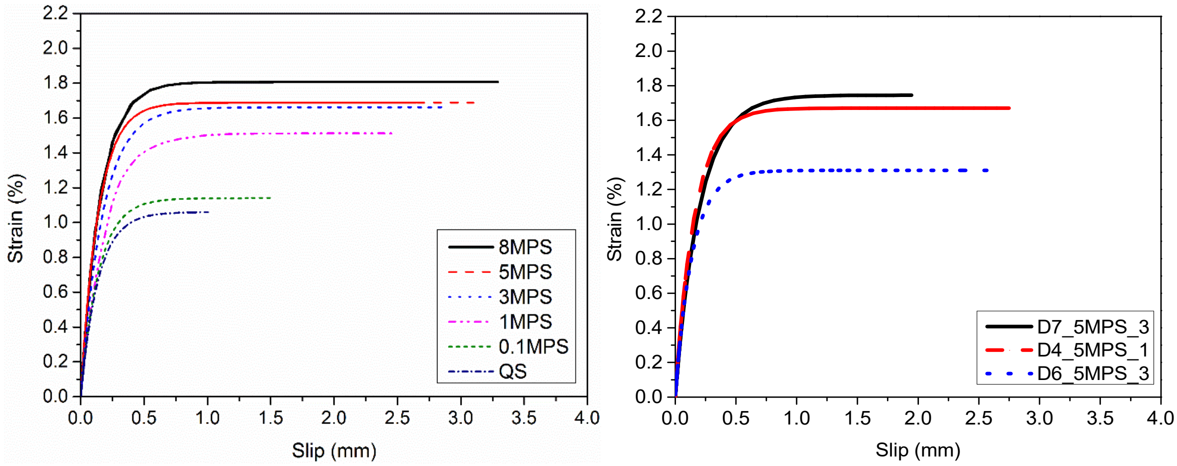

Figure 12. Strain-slip curves for the specimens under different loading speeds

3.5 Strain profile and effective bond length

EBL is the distance of stress transfer zone along which most of the bond shear stress is transmitted into the concrete [51]. Three regions can be observed in the measured strain distribution: (1) fully debonded stage near the loaded end; (2) bond shear stress transferring stage; and (3) unstressed stage near the free end. In addition, EBL can be obtained through the strain distribution derived from the DIC technique [35].

As shown in Figure 13, successive digital images were prepared and analyzed using DIC and the longitudinal strain profile at each loading level was obtained. The averaged EBL at 8 m/s was 47.7 mm which is lower than 91 mm at 0.1 m/s. This indicates that the EBL decreased with the raising strain rate, which is evident with the steeper strain distribution gradient in Figure 13. The steeper strain distribution gradient indicates the shorter distance of the shear stress transferring zone. **Table 1** gives the EBLs for all the tested specimens. The averaged EBLs for specimens QS, D1_0.1MPS, D2_1MPS, D3_3MPS, D4_5MPS, and D5_8MPS are 92.5 mm, 91 mm, 66.3 mm, 63.3 mm, 51 mm, and 47.7mm, respectively. As the strain rate raised from 2.59E-5 s^{-1} to 4.27 s^{-1}, 29.47 s^{-1}, 51.47 s^{-1}, 103.17 s^{-1}, and 155.10 s^{-1}, the dynamic EBL decreased by 1.62%, 28.29%, 31.53%, 44.86%, and 48.46%, respectively. In addition, changing the BFRP sheets from two layers to four layers resulted in the increasing effective bond length under static loadings due to the increased BFRP stiffness ($E_f t_f$). For the specimens with four layers of BFRP sheets, the EBL decreased with the strain rate, which is the same as the specimens with two BFRP layers under dynamic loadings. The test results show that the descent rate after the loading speed of 3 m/s is slow indicating that the strain rate effect has a certain range of influence on the EBL, which agrees with the conclusions by Shen et al. [32] and Huo et al. [33].

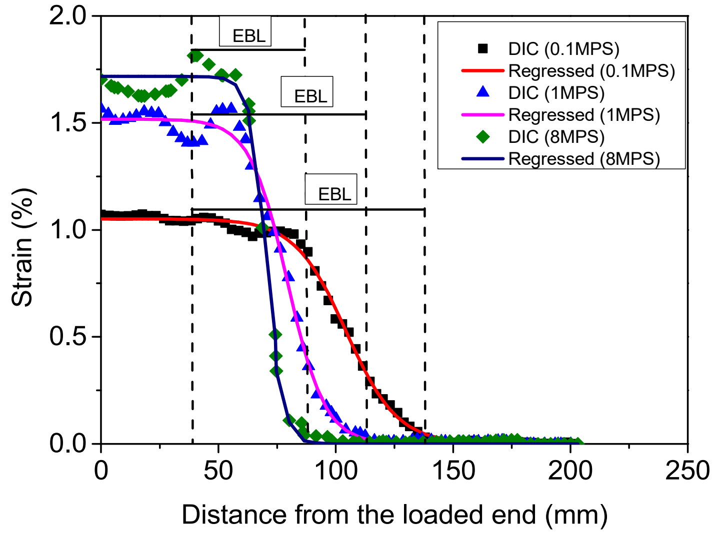

Figure 13. EBL under different loading speeds

3.6 Interfacial bond stress-slip relationship

The shear stress and the slip can be obtained by imposing the equilibrium condition of FRP sheets with the infinite length. The shear stress and slip can be obtained by the following equations:

$$\tau = E_f t_f \frac{df(s)}{ds} f(s) \quad (5)$$

where $f(s)$ is the function of slip (s).

$$\frac{df(s)}{ds} = ABe^{-Bs} \quad (6)$$

By substituting Equation (6) into Equation (5), the interfacial bond-slip relationship can be expressed as a function of *A* and *B* as follows [16]:

$$\tau = A^2 B E_f t_f (\mathrm{e}^{-Bs} - \mathrm{e}^{-2Bs}) \quad (7)$$

The IFE G_f is defined as follows:

$$G_f = \int_0^{\infty} \tau ds \quad (8)$$

By substituting Equation (7) into Equation (8), G_f can be yielded:

$$G_f = \frac{1}{2} A^2 E_f t_f \quad (9)$$

The coefficients *A* and *B* can be obtained by fitting the strains-slip curves in section 3.3. Figure 14 shows the fitted interfacial bond stress-slip curves at various loading rates. Table 1 gives the experimental results of PSS and the corresponding slip. It is obvious that the PSS raised remarkably with strain rate. The average PSS of specimens D1_0.1MPS, D2_1MPS, D3_3MPS, D4_5MPS, and D5_8MPS are 2.76 MPa, 5.03 MPa, 7.04 MPa, 8.32 MPa, and 9.47 MPa, respectively. It can be observed that the IFE increases with the strain rate as well, which is defined as the enclosed area of bond-slip curve. The average IFE of specimens of D1_0.1MPS, D2_1MPS, D3_3MPS, D4_5MPS, and D5_8MPS are 1.05 N/mm, 1.86 N/mm, 2.40 N/mm, 2.48 N/mm, and 2.73 N/mm, respectively. The reason for the increment of the IFE is because the shear modulus of concrete, adhesive and FRP increased with the strain rate and the interfacial stiffness *K* increases with the shear modulus according to Equations (2) and (3). The increase of PSS is mainly due to the increment of IFE.

To verify the dynamic interfacial shear stress of the BFRP-to-concrete interface, the dynamic tensile strength of concrete corresponding to the strain rate was estimated to compare with the interfacial shear stress because of stripping of the concrete layers. There was no normal stress applied in the single-lap shear test, shear stress penetrated into the concrete with a 45° angle and consequently the debonding always initiated on the tensile side of concrete substrate. The dynamic increase factor (DIF) of the concrete was employed herein to obtain the dynamic tensile strength of the concrete substrates ($f_{t,DIF}$) [52], as summarized in Table 1. It can be observed that the estimated dynamic tensile strength of the concrete substrates is close to the interfacial shear stress of the BFRP-to-concrete interfaces, indicating that the obtained PSS is reasonable and consistent with the tensile strength increment of concrete material with strain rate.

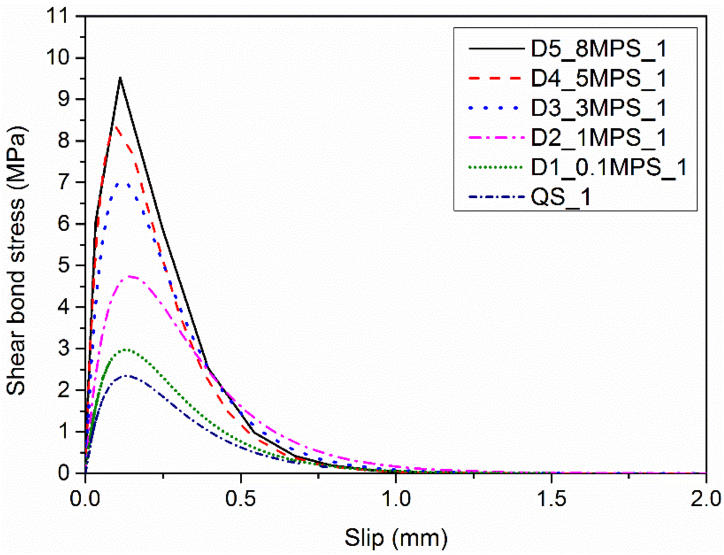

Figure 14. Fitted bond-slip curves under different loading speeds

4 Theoretical predictions and proposed models

4.1 Effect of strain rate on IFE

Figure 15 shows the relationship of the IFE against strain rate. As the IFE increases with the strain rate, the relationship between $G_{f,d}$ and $G_{f,s}$ can be established by incorporating strain rate effect. Yen and Caiazzo [53] proposed logarithmic functions to define the strain rate effects on the mechanical properties of composites. Shen et al. [54] also used logarithmic functions to describe the relationship between strain rate and bond properties of BFRP-to-concrete interface. Thus, the non-linear logarithmic function is employed herein to describe the impact of strain rate on the interfacial bond properties. After regression analysis, empirical equations incorporating strain rate effect are given below:

$$\frac{G_{f,d}}{G_{f,s}} = 1 + 3.354\times10^{-5}\left(\log(\frac{\dot{\varepsilon}_d}{\dot{\varepsilon}_s})\right)^{5.881} \quad \text{when } 2.5\times10^{-5} \le \dot{\varepsilon} \le 155.10 \qquad (10)$$

where $G_{f,d}$ and $G_{f,s}$ refer to the dynamic and static interfacial fracture energy, respectively; $\dot{\varepsilon}_d$ and $\dot{\varepsilon}_s$ refer to the dynamic and static strain rate, respectively.

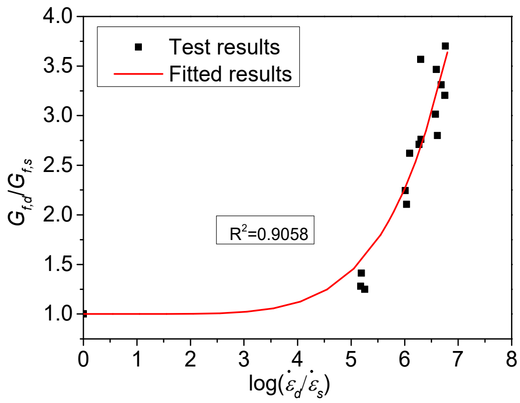

Figure 15. Relationship between IFE and strain rate

Dai et al. [16] proposed an equation to predict the $G_{f,s}$ considering the concrete compressive strength (f_c'), FRP stiffness ($E_f t_f$), and interfacial stiffness (G_a/t_a). As the shear modulus of concrete, adhesive, and BFRP (i.e. G_c, G_a and G_F) together determine the interfacial stiffness, these factors (i.e. G_c, G_a and G_F) are incorporated into the interfacial stiffness (K) and consequently the static interfacial fracture energy ($G_{f,s}$). Then the effect of strain rate is incorporated into the proposed static model to obtain the dynamic interfacial fracture energy. The proposed model is given below:

$$G_{f,s} = \varphi \left(E_f t_f \right)^{\theta} K^{C} \tag{11}$$

$$K = \frac{\frac{G_c}{t_c} \frac{G_a}{t_a} \frac{G_F}{t_f}}{\frac{G_c}{t_c} + \frac{G_a}{t_a} + \frac{G_F}{t_F}} \tag{12}$$

where φ, θ, and C are coefficients determined from the data collection [19]. After regression analysis according to the testing data, the coefficients are determined, and the static IFE is given as:

$$G_{f,s} = 0.345 \left(E_f t_f \right)^{0.029} K^{-0.986} \tag{13}$$

By substituting Equations (11), (12) and (13) into Equation (10), the dynamic interfacial fracture energy $G_{f,d}$ can be predicted by incorporating strain rate effect. It should be noted that the thickness of concrete t_c = 20 mm was selected according to [46]. The thickness of concrete should be 2 or 3 times the aggregate size [55]. E_c was determined by using $E_c = 4700\sqrt{f_c^{'}}$ [56].

4.2 Effect of strain rate on bond strength

Figure 16 shows the relationship of the debonding load P_u against strain rate. As the debonding load increases with the strain rate, the relation between dynamic and static debonding loads ($P_{u,d}$ and $P_{u.s}$) can be established by incorporating the effects of strain rate. After regression analysis, empirical equation incorporating strain rate effect is given below:

$$\frac{P_{u,d}}{P_{u,s}} = 1 + 1.444 \times 10^{-10} \left(\log(\frac{\dot{\varepsilon}_d}{\dot{\varepsilon}_s}) \right)^{11.74} \quad \text{when } 2.5 \times 10^{-5} \le \dot{\varepsilon} \le 155.10 \tag{14}$$

The debonding load can be expressed by considering the IFE, which has been widely applied in estimating the interfacial debonding loads [19, 44, 47]. The $G_{f,s}$ can be expressed by Equation (13) and the static debonding load ($P_{u.s}$) is given as:

$$P_{u,s} = b_f \sqrt{2E_f t_f G_{f,s}} \quad (15)$$

By substituting Equations (10) and (15) into Equation (14), the dynamic debonding load ($P_{u,d}$) can be obtained.

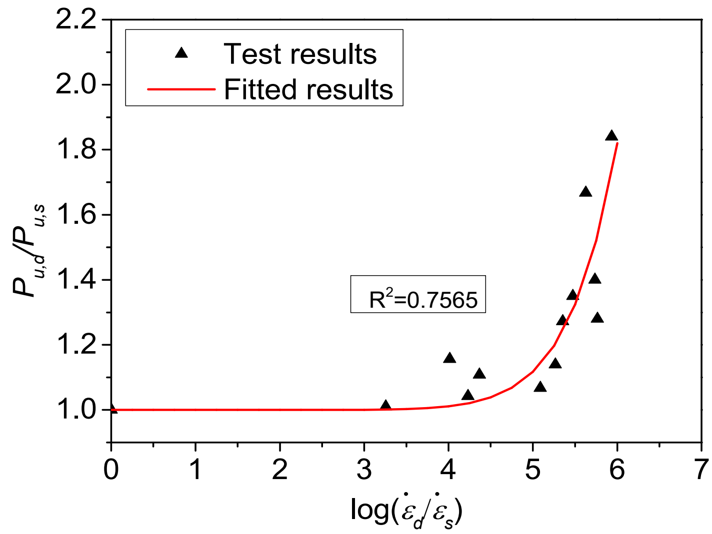

Figure 16. DIF of debonding load

4.3 Effect of strain rate on interfacial shear stress and slip

As discussed in section 3.4, two coefficients (i.e. G_f and B) can be obtained from the fitted strain-slip relationship. According to the previous model [16], both the IFE and the stiffness index B determine the bond stress-slip relationship.

$$\tau = 2BG_f\left(e^{-Bs} - e^{-2Bs}\right) \quad (16)$$

$$\tau_{\max} = \frac{1}{2}BG_f \quad (17)$$

$$s_{\max} = \frac{In2}{B} = \frac{0.693}{B} \quad (18)$$

As the stiffness index B increases with the strain rate, and using the testing results given in **Table 1**, the dynamic stiffness index B_d by incorporating strain rate can be expressed by Equation (20). The relationship between the static stiffness index (B_s) and the mechanical properties of FRP, epoxy and concrete can be expressed by Equation (19). After regression analysis, the stiffness index model is proposed as Equation (20).

$$B_s = 5.908\left(E_f t_f\right)^{0.108} K^{0.833} \tag{19}$$

$$\frac{B_d}{B_s} = 1 + 2.963\times10^{-10}\left(\log(\frac{\dot{\varepsilon}_d}{\dot{\varepsilon}_s})\right)^{11.03} \quad \text{when } 2.5\times10^{-5} \le \dot{\varepsilon} \le 155.10 \tag{20}$$

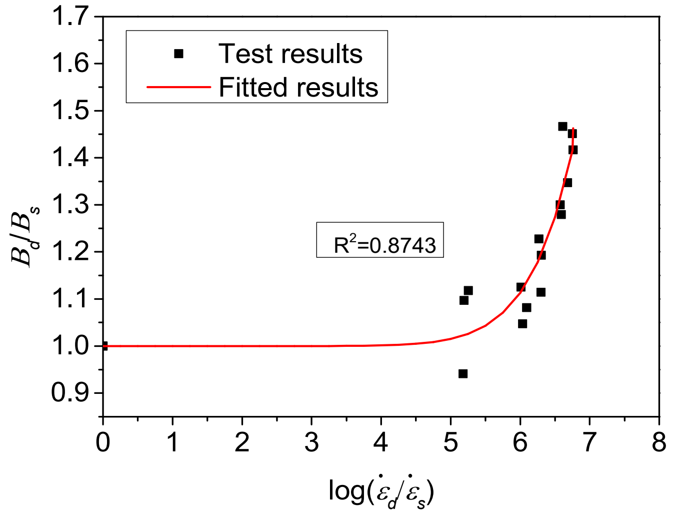

Figure 17. Relationship between stiffness index and strain rate

The PSS τ_m and the corresponding slip s_o are two critical factors determining the bond-slip response. The test results showed that the PSS increased while the corresponding slip decreased with the rising strain rate. After regression analysis, the τ_m and s_o can be obtained by the following equations:

$$\frac{\tau_{m,d}}{\tau_{m,s}} = 1 + 1.328\times10^{-6}\left(\log(\frac{\dot{\varepsilon}_d}{\dot{\varepsilon}_s})\right)^{7.795} \quad \text{when } 2.5\times10^{-5} \le \dot{\varepsilon} \le 155.10 \tag{21}$$

$$\frac{s_{o,d}}{s_{o,s}} = 1 - 6.618\times10^{-9}\left(\log(\frac{\dot{\varepsilon}_d}{\dot{\varepsilon}_s})\right)^{9.226} \quad \text{when } 2.5\times10^{-5} \le \dot{\varepsilon} \le 155.10 \tag{22}$$

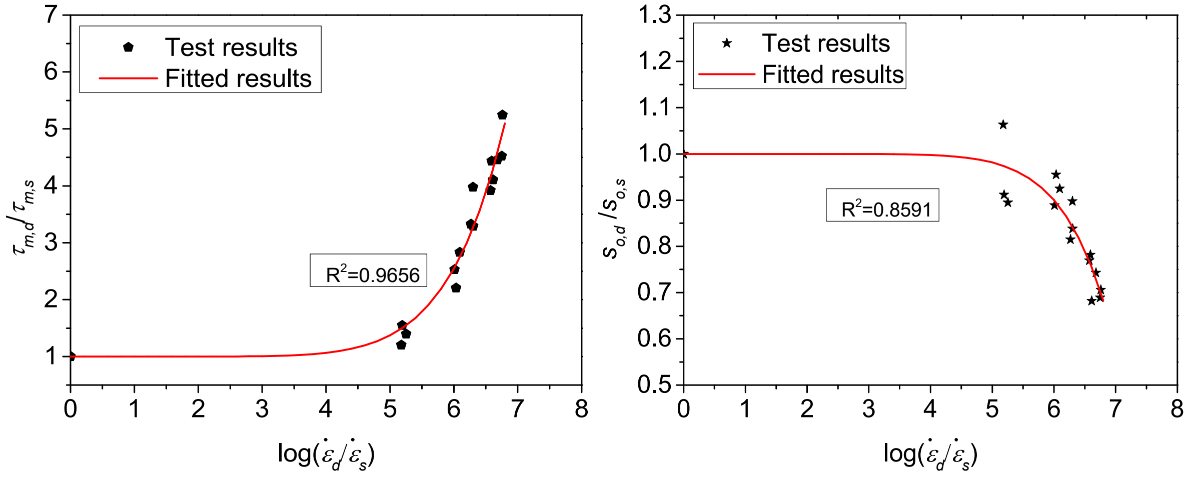

(a) PSS (b) Slip at PSS

Figure 18. Relationship between (a) peak shear stress vs. strain rate; (b) slip vs. strain rate

By substituting Equations (10) and (20) into Equation (17) and substituting Equations (19) and (20) into Equation (18), the dynamic PSS $\tau_{m,d}$ and the corresponding slip $s_{o,d}$ can be obtained. Additionally, the dynamic bond-slip relationships can be determined by substituting Equations (10), (17), (18) and (20) into Equation (16). Figure 19 plots the comparison of the predicted and tested bond-slip curves. It should be noted that all the proposed models in this study are applicable for the strain rate ranging between $2.5\text{x}10^{-5}$ s^{-1} and 155.10 s^{-1}.

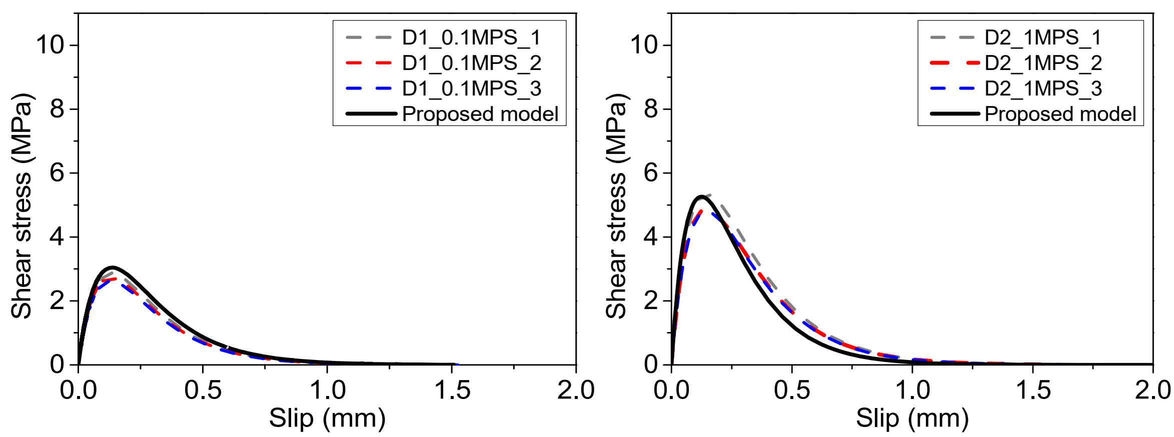

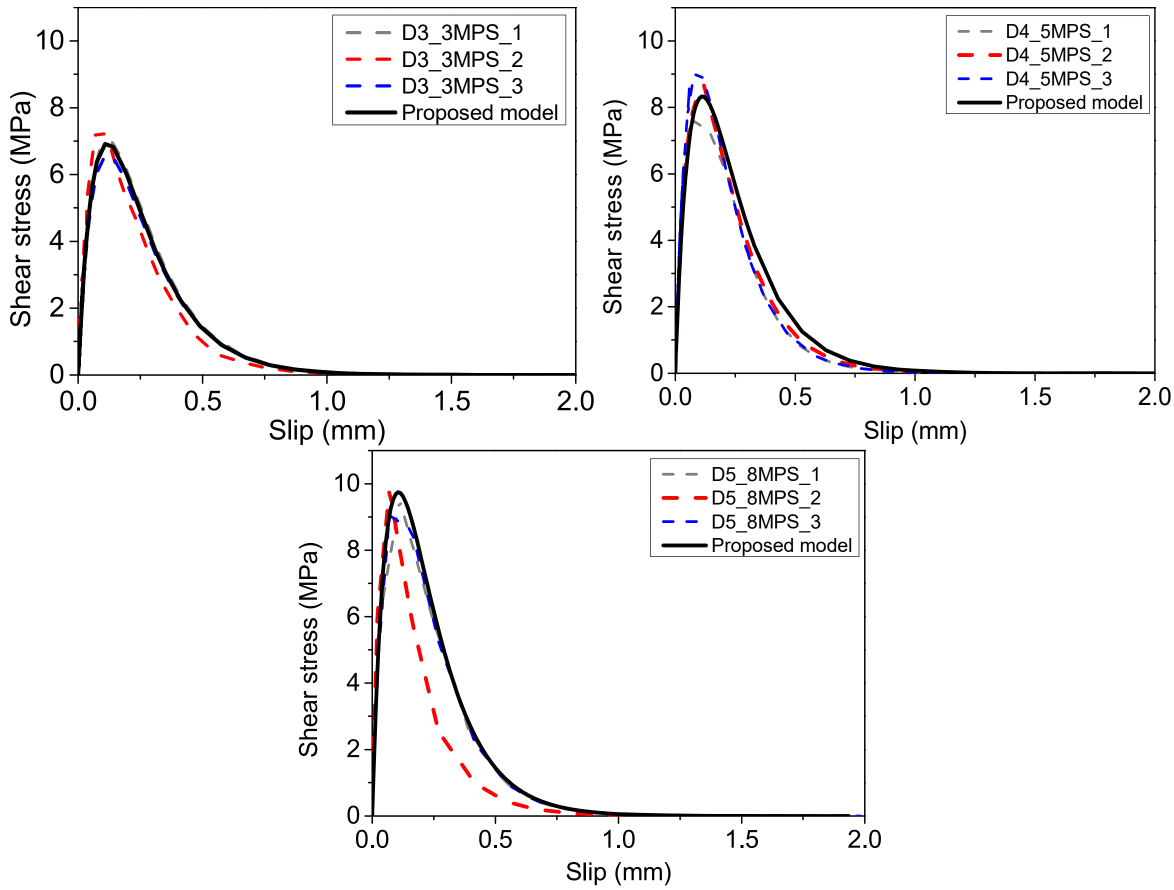

Figure 19. Predicted vs. tested bond-slip curves

4.4 Validation of the proposed dynamic models

The proposed dynamic bond-slip model can be used to determine the debonding load, the PSS, the BFRP strain distribution and the bond-slip curve. Testing results can directly provide the debonding load and FRP strain distribution. In this section, the present and previous testing data were collected to compare with the predicted results. As there were limited experimental studies in the literature regarding the dynamic interfacial bond of FRP-to-concrete interface, two studies by Huo et al. [33] and Shen et al. [32] are selected to validate the predictions. Figure 20 shows the comparisons of the predicted and tested results. The experimental results from the present study and the study of Shen et al. [32] match well with the predicted results. However, the experimental results by Huo et al. [33] is overestimated by the proposed model. The discrepancies might be due to different testing methods. Huo et al. [33] used the testing method of three-point impact tests on beams bonded by FRP for dynamic bonding test and consequently the additional bending moment and normal stress complicated the debonding process. However, Shen et al. [32] employed double-lap shear test method and the present study used single-lap shear test method to investigate dynamic bonding behaviours.

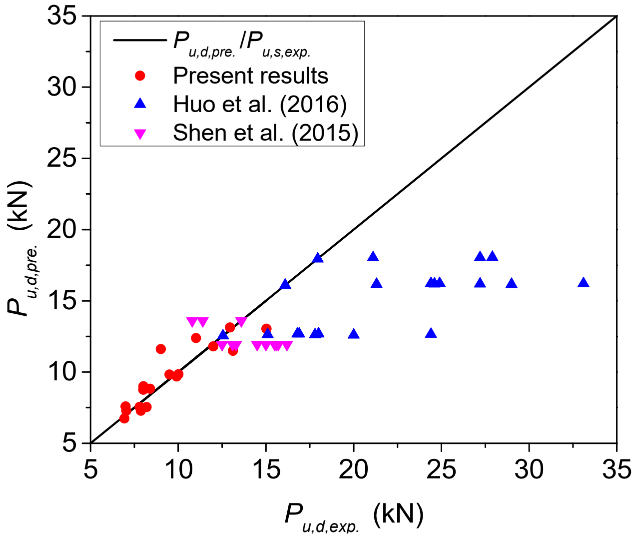

Figure 20. Experimental results vs. predicted results

The FRP strain distributions along the bonded length can be obtained by the proposed bond-slip model based on the studies from Zhou et al. [10] and Yuan et al. [15]. Analytical studies were carried out by Zhou et al. [10] and Yuan et al. [15] on the full debonding process of FRP-to-concrete joints, and consequently the strain distributions at various loading levels were predicted based on the proposed models. Figure 21 illustrates the comparison between the tested and predicted FRP strain distributions of four specimens. The Specimen D4_5MPS_1 and D5_8MPS_1) are selected from the present study, and it is noted that the BFRP strains were measured by the DIC method. Other two specimens (i.e. L200-D3-2 and L200-D2-1) were tested by Shen et al. [32], and the BFRP strains were measured by the strain gauges. Comparisons show that the predicted strain distributions match well with the tested results at different dynamic loading stages. The proposed model can properly predict the pre-debonding stage and post-debonding stage, and the predicted strain profile remained the same shape to propagate the debonding process. The experimental strain distributions of Huo et al. [33] were not compared herein due to different testing method and different FRP materials.

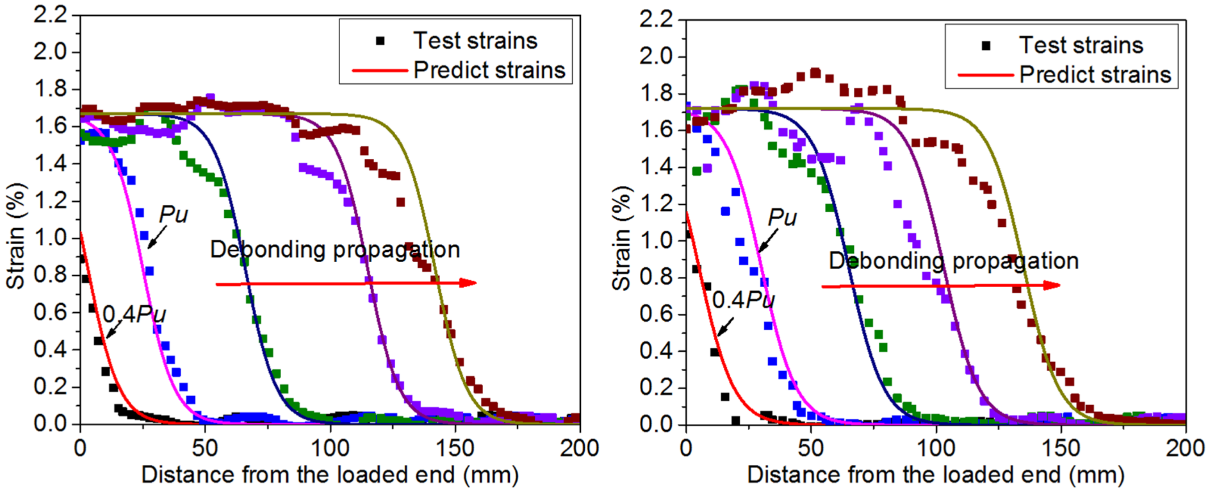

(a) Specimen D4_5MPS_1 (present study) (b) Specimen D5_8MPS_1 (present study)

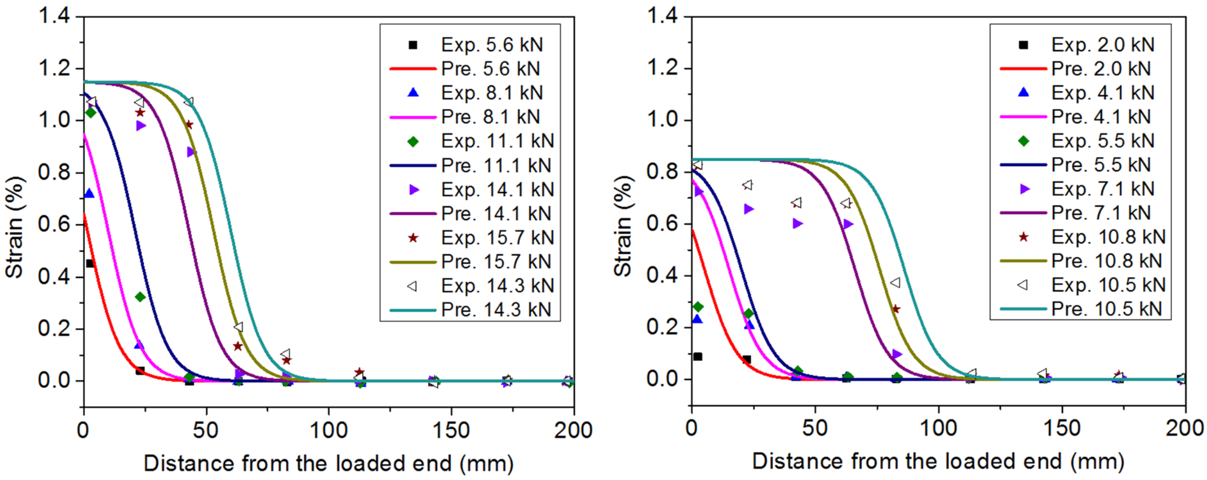

(c) Specimen L200-D3-2 (Shen et al. 2015) (d) Specimen L200-D2-1 (Shen et al. 2015)

Figure 21. Comparison between the tested and predicted strain distributions

5 Conclusions

This study experimentally investigates the strain rate effect on the failure modes, strain distributions, interfacial fracture energy, strain-slip response, debonding load, and bond-slip response by implementing SST. The following conclusions can be drawn:

(1) Strain rate changed the failure modes of the BFRP-to-concrete interface. Two debonding failure modes of the BFRP-to-concrete interface under dynamic loadings can be observed,

i.e. debonding in concrete failure (C) and debonding in the interface of concrete-epoxy (CE).

(2) The single-lap shear specimens under dynamic loadings exhibited more ductile behaviour due to the increased ultimate slip. The shear slip increased by 13.89%, 32.61%, 34.97%, 52.06%, and 58.48% with the rising strain rate from $2.5\text{x}10^{-5}$ s^{-1} to 4.27 s^{-1}, 29.47 s^{-1}, 51.47 s^{-1}, 103.17 s^{-1}, and 155.10 s^{-1}, respectively. The increased slippages at the interface improved the interfacial fracture energy and consequently the bond strength of the interface.

(3) The strain distributions in BFRP sheets were significantly affected by the dynamic loadings. The strain distribution gradient in the BFRP sheets under higher loading speeds was steeper than those obtained with lower loading speed. By changing the BFRP sheets from two layers to four layers, the debonding strain of BFRP sheets reduced due to the increased FRP thickness. Reducing the bonding width of BFRP sheets from 40 mm to 25 mm had little effect on the interfacial stiffness while the ultimate debonding strain increased under dynamic loadings.

(4) The dynamic effective bond length (EBL) decreased with the increasing strain rate, but the effect of strain rate on the EBL became less prominent when subjected to relatively higher loading rate, such as 5 m/s and 8 m/s.

(5) By comparing the predicted results with the testing data, the validated proposed dynamic bond-slip model by incorporating the strain rate can accurately predict the dynamic bond behaviour of BFRP-to-concrete interface.

Acknowledgements

The authors thank Australian Research Council Linkage Project (ARC LP150100259) for the financial support.

References

[1] W. Chen, T.M. Pham, H. Sichembe, L. Chen, H. Hao. Experimental Study of Flexural Behaviour of Rc Beams Strengthened by Longitudinal and U-Shaped Basalt Frp Sheet. Compos B Eng (2017).

[2] T.M. Pham, H. Hao. Impact Behavior of Frp-Strengthened Rc Beams without Stirrups. J Compos Constr 20 (4) (2016) 04016011.

[3] Y.-F. Wu, C. Jiang. Effect of Load Eccentricity on the Stress–Strain Relationship of Frp-Confined Concrete Columns. Compos Struct 98 (2013) 228-41.

[4] J. Teng, J.-F. Chen, S.T. Smith, L. Lam. Frp: Strengthened Rc Structures. AIP Conf Proc (2002) 266.

[5] H.M. Diab, O.A. Farghal. Bond Strength and Effective Bond Length of Frp Sheets/Plates Bonded to Concrete Considering the Type of Adhesive Layer. Compos B Eng 58 (2014) 618-24.

[6] B. Wan, C. Jiang, Y.-F. Wu. Effect of Defects in Externally Bonded Frp Reinforced Concrete. Constr Build Mater 172 (2018) 63-76.

[7] S. Hadigheh, R. Gravina, S. Setunge. Prediction of the Bond–Slip Law in Externally Laminated Concrete Substrates by an Analytical Based Nonlinear Approach. Materials & Design (1980-2015) 66 (2015) 217-26.

[8] H. Diab, Z. Wu. Nonlinear Constitutive Model for Time-Dependent Behavior of Frp-Concrete Interface. Composites science and technology 67 (11-12) (2007) 2323-33.

[9] D. Bruno, R. Carpino, F. Greco. Modelling of Mixed Mode Debonding in Externally Frp Reinforced Beams. Composites science and technology 67 (7-8) (2007) 1459-74.

[10] Y.-W. Zhou, Y.-F. Wu, Y. Yun. Analytical Modeling of the Bond–Slip Relationship at Frp-Concrete Interfaces for Adhesively-Bonded Joints. Compos B Eng 41 (6) (2010) 423-33.

[11] Z. Wu, S. Islam, H. Said. A Three-Parameter Bond Strength Model for Frp—Concrete Interface. J Reinf Plast Comp 28 (19) (2009) 2309-23.

[12] Z. Wu, H. Yuan, Y. Kojima, E. Ahmed. Experimental and Analytical Studies on Peeling and Spalling Resistance of Unidirectional Frp Sheets Bonded to Concrete. Composites science and technology 65 (7-8) (2005) 1088-97.

[13] D. Zhang, X.-L. Gu, Q.-Q. Yu, H. Huang, B. Wan, C. Jiang. Fully Probabilistic Analysis of Frp-to-Concrete Bonded Joints Considering Model Uncertainty. Compos Struct 185 (2018) 786-806.

[14] J. Vaculik, P. Visintin, N. Burton, M. Griffith, R. Seracino. Constr Build Mater 183 (2018) 325-45.

[15] H. Yuan, J. Teng, R. Seracino, Z. Wu, J. Yao. Full-Range Behavior of Frp-to-Concrete Bonded Joints. Eng Struct 26 (5) (2004) 553-65.

[16] J.G. Dai, T. Ueda, Y. Sato. Development of the Nonlinear Bond Stress–Slip Model of Fiber Reinforced Plastics Sheet–Concrete Interfaces with a Simple Method. J Compos Constr 9 (1) (2005) 52-62.

[17] J. Dai, T. Ueda, Y. Sato. Bonding Characteristics of Fiber-Reinforced Polymer Sheet-Concrete Interfaces under Dowel Load. J Compos Constr 11 (2) (2007) 138-48.

[18] Y.-F. Wu, X.-S. Xu, J.-B. Sun, C. Jiang. Analytical Solution for the Bond Strength of Externally Bonded Reinforcement. Compos Struct 94 (11) (2012) 3232-9.

[19] Y.-F. Wu, C. Jiang. Quantification of Bond-Slip Relationship for Externally Bonded Frp-to-Concrete Joints. J Compos Constr 17 (5) (2013) 673-86.

[20] C. Yuan, W. Chen, T.M. Pham, H. Hao. Effect of Aggregate Size on Bond Behaviour between Basalt Fibre Reinforced Polymer Sheets and Concrete. Compos B Eng 158 (2019) 459-74.

[21] P. Buchan, J. Chen. Blast Resistance of Frp Composites and Polymer Strengthened Concrete and Masonry Structures–a State-of-the-Art Review. Compos B Eng 38 (5-6) (2007) 509-22.
[22] H. Hao. Reliability Analysis of Rc Slabs with or without Frp Strengthening to Blast Loads. (2014).
[23] H. Hao, E.K. Tang. Numerical Simulation of a Cable-Stayed Bridge Response to Blast Loads, Part Ii: Damage Prediction and Frp Strengthening. Eng Struct 32 (10) (2010) 3193-205.
[24] A.A. Mutalib, H. Hao. Development of Pi Diagrams for Frp Strengthened Rc Columns. International journal of impact engineering 38 (5) (2011) 290-304.
[25] T.M. Pham, H. Hao. Behavior of Fiber-Reinforced Polymer-Strengthened Reinforced Concrete Beams under Static and Impact Loads. International Journal of Protective Structures 8 (1) (2017) 3-24.
[26] T.M. Pham, H. Hao. Plastic Hinges and Inertia Forces in Rc Beams under Impact Loads. International Journal of Impact Engineering 103 (2017) 1-11.
[27] D. Grote, S. Park, M. Zhou. Dynamic Behavior of Concrete at High Strain Rates and Pressures: I. Experimental Characterization. International Journal of Impact Engineering 25 (9) (2001) 869-86.
[28] O. Okoli, G. Smith. The Effect of Strain Rate and Fibre Content on the Poisson's Ratio of Glass/Epoxy Composites. Compos Struct 48 (1-3) (2000) 157-61.
[29] T.M. Pham, H. Hao. Review of Concrete Structures Strengthened with Frp against Impact Loading. Structures: Elsevier; 2016. p. 59-70.
[30] J. Cui, H. Hao, Y. Shi. Discussion on the Suitability of Concrete Constitutive Models for High-Rate Response Predictions of Rc Structures. International Journal of Impact Engineering 106 (2017) 202-16.
[31] J.W. Shi, H. Zhu, Z.S. Wu, G. Wu. Experimental Study of the Strain Rate Effect of Frp Sheet-Concrete Interface. China Civil Eng J 45 (12) (2012) 99-107.
[32] D. Shen, H. Shi, Y. Ji, F. Yin. Strain Rate Effect on Effective Bond Length of Basalt Frp Sheet Bonded to Concrete. Constr Build Mater 82 (2015) 206-18.
[33] J. Huo, J. Liu, X. Dai, J. Yang, Y. Lu, Y. Xiao, G. Monti. Experimental Study on Dynamic Behavior of Cfrp-to-Concrete Interface. J Compos Constr 20 (5) (2016) 04016026.
[34] C. Yuan, W. Chen, T.M. Pham, H. Hao, J. Cui, Y.C. Shi. Strain Rate Effect on Interfacial Bond Behaviour between Bfrp Sheets and Steel Fibre Reinforced Concrete. Compos B Eng (2019).
[35] C. Yuan, W. Chen, T.M. Pham, H. Hao. Bond Behavior between Basalt Fibres Reinforced Polymer Sheets and Steel Fibres Reinforced Concrete. Eng Struct 176 (2018) 812-24.
[36] Y. Xia, J. Zhu, K. Wang, Q. Zhou. Design and Verification of a Strain Gauge Based Load Sensor for Medium-Speed Dynamic Tests with a Hydraulic Test Machine. International Journal of Impact Engineering 88 (2016) 139-52.
[37] J. Li, X. Fang. Stress Wave Analysis and Optical Force Measurement of Servo-Hydraulic Machine for High Strain Rate Testing. Experimental Mechanics 54 (8) (2014) 1497-501.
[38] H.A. Baky, U. Ebead, K. Neale. Nonlinear Micromechanics-Based Bond–Slip Model for Frp/Concrete Interfaces. Eng Struct 39 (2012) 11-23.
[39] X. Xiao. Dynamic Tensile Testing of Plastic Materials. Polymer Testing 27 (2) (2008) 164-78.
[40] W. Chen, H. Hao, D. Hughes, Y. Shi, J. Cui, Z.-X. Li. Static and Dynamic Mechanical Properties of Expanded Polystyrene. Materials & Design 69 (2015) 170-80.
[41] J. Fitoussi, F. Meraghni, Z. Jendli, G. Hug, D. Baptiste. Experimental Methodology for High Strain-Rates Tensile Behaviour Analysis of Polymer Matrix Composites. Composites Science and Technology 65 (14) (2005) 2174-88.

[42] B.L. Boyce, M.F. Dilmore. The Dynamic Tensile Behavior of Tough, Ultrahigh-Strength Steels at Strain-Rates from 0.0002 S− 1 to 200 S− 1. International Journal of Impact Engineering 36 (2) (2009) 263-71.
[43] J.G. Dai, T. Ueda, Y. Sato. Bonding Characteristics of Fiber-Reinforced Polymer Sheet-Concrete Interfaces under Dowel Load. J Compos Constr 11 (2) (2007) 138-48.
[44] H.C. Biscaia, C. Chastre, I.S. Borba, C. Silva, D. Cruz. Experimental Evaluation of Bonding between Cfrp Laminates and Different Structural Materials. J Compos Constr 20 (3) (2015) 04015070.
[45] K.V. Subramaniam, C. Carloni, L. Nobile. Width Effect in the Interface Fracture During Shear Debonding of Frp Sheets from Concrete. Eng Struct 74 (4) (2007) 578-94.
[46] N.R. Council. Guide for the Design and Construction of Externally Bonded Frp Systems for Strengthening Existing Structures. CNR-DT200 (2013).
[47] Y. Pan, G. Xian, H. Li. Effects of Freeze-Thaw Cycles on the Behavior of the Bond between Cfrp Plates and Concrete Substrates. J Compos Constr 22 (3) (2018) 04018011.
[48] L. Liao, T. Kobayashi, T. Sawa, Y. Goda. 3-D Fem Stress Analysis and Strength Evaluation of Single-Lap Adhesive Joints Subjected to Impact Tensile Loads. Int J Adhes Adhes 31 (7) (2011) 612-9.
[49] Y. Hao, H. Hao. Dynamic Compressive Behaviour of Spiral Steel Fibre Reinforced Concrete in Split Hopkinson Pressure Bar Tests. Constr Build Mater 48 (2013) 521-32.
[50] W. Chen, H. Hao, M. Jong, J. Cui, Y. Shi, L. Chen, T.M. Pham. Quasi-Static and Dynamic Tensile Properties of Basalt Fibre Reinforced Polymer. Compos B Eng 125 (2017) 123-33.
[51] A. Franco, G. Royer-Carfagni. Effective Bond Length of Frp Stiffeners. Int J Nonlin Mech 60 (2014) 46-57.
[52] Y. Hao, H. Hao, X. Zhang. Numerical Analysis of Concrete Material Properties at High Strain Rate under Direct Tension. International Journal of Impact Engineering 39 (1) (2012) 51-62.
[53] C.F. Yen, A. Caiazzo. Innovative Processing of Multifunctional Composite Armor for Ground Vehicles. Arl Technical Report Arl-Cr-484. US Army Research Laboratory, Aberdeen Proving Ground, MD; 2000.
[54] D. Shen, Y. Ji, F. Yin, J. Zhang. Dynamic Bond Stress-Slip Relationship between Basalt Frp Sheet and Concrete under Initial Static Loading. J Compos Constr 19 (6) (2015) 04015012.
[55] B. Ferracuti, M. Savoia, C. Mazzotti. Interface Law for Frp–Concrete Delamination. Compos Struct 80 (4) (2007) 523-31.
[56] A. Committee, A.C. Institute, I.O.f. Standardization. Building Code Requirements for Structural Concrete (Aci 318-08) and Commentary. American Concrete Institute; 2008.